The University of Nottingham

UNITED KINGDOM · CHINA · MALAYSIA

Petkov, Markian P. and Hyde, Christopher J. and Hyde, Thomas H. (2016) Practical considerations of the use of cross-weld and compact tension specimens creep data. Journal of Strain Analysis for Engineering Design, 51 (3). pp. 179-206. ISSN 0309-3247

Access from the University of Nottingham repository:
http://eprints.nottingham.ac.uk/35546/1/Petkov_Hyde_Hyde_Practical%20considerations%20of%20the%20use%20of%20cross-weld%20and%20compact%20tension%20specimens%20creep%20data.pdf

Practical considerations of the use of cross-weld and compact tension specimens creep data

Markian P Petkov, Christopher J Hyde and Thomas H Hyde
Department of Mechanical, Materials and Manufacturing Engineering, University of Nottingham, UK
Corresponding author:
Markian Petkov Petkov, Department of Mechanical, Materials and Manufacturing Engineering, University of Nottingham, Nottingham, NG7 2RD, United Kingdom.
Email: markianpetkov@gmail.com

Keywords: creep, creep data, cross-weld, compact tension, creep crack growth, C*-integral, damage mechanics, fracture

Abstract

The present article gives an overview of the use of cross-weld and compact tension specimen modelling and analyses data to characterise creep behaviour of high temperature components. Cross-weld and CT specimens are used to describe creep crack growth in heterogeneous material structures, such as welds, and a number of factors that affect the creep behaviour of the structure, associated with this heterogeneity, have been identified. Creep data obtained from cross-weld specimen modelling is substantially affected by the material model used (e.g. Norton Power law, Liu/Murakami model, etc.), stress singularities that arise at the material interfaces and in between the columnar and equiaxed zones of the weld material, residual stresses which arise though the thickness of a multi-pass weld and the extraction orientation of the specimen relative to the welding direction. Creep crack growth data obtained from CT specimen testing and analyses is strongly dependent on the material models used (isotropic hardening models, Norton Creep law, Liu/Murakami model, etc.), the path-dependence of the C*-contour integral fracture parameter for certain heterogeneous material configurations and the accurate computation of material constants for damage mechanics models, and the agreement between loading state to the actual stress state of the component to which the CT specimen creep data is applied to. The present study examines typical results and observations from cross-weld specimen and CT specimen creep analyses, identifying the advantages, disadvantages and limitations of each specimen procedure.

Nomenclature

Latin letters

a	crack length
$\dot{a}$	crack growth rate (da/dt)
A	material constant (Kachanov damage or Norton creep law)
B	material constant (Kachanov damage or Norton creep law)
B_N	CT specimen thickness
C	material constant (Liu/Murakami damage model)
$C^*, C(t)$	steady-state contour integral, transient contour integral
$CMOD$	crack mouth opening displacement
d	diameter of cross-weld specimen
D	material constant
D_{gb}	grain boundary diffusion
E	Young's modulus
h	height of weld material zone (Adjusted C*-integral expression)
H^{LLD}	function of the creep exponent (n)
I_n	hardening exponent dependent constant (HRR)
J_V	cavity flux
k	Stefan-Boltzmann constant
K_I	stress intensity factor (Mode I)
K_{app}	stress intensity factor (due to loading)
K_{res}	stress intensity factor (residual stress)
K_{ij}, K_{eq}	stress variation functions (singularity functions)
m	material constant (Kachanov damage model)
MSR	minimum strain rate
n	creep exponent (Norton creep law); material constant (Kachanov model)
n_{eq}	equivalent creep exponent
n_2	material exponent (Liu/Murakami damage model)
N_{ij}, N_{eq}	singularity exponents (direct, shear and equivalent)
NG	narrow gap weld

p	material constant (Liu/Murakami damage model)
p_i	internal pressure
P	load applied
q	exponent (a-C* method)
q_1, q_2	material constants (damage models)
r_p	radius of plastic zone
S	contour path
S_{ij}	deviatoric stress
t	time
t_f	failure time
t_τ	transition time to uniform creep behaviour
T	temperature
T_{ij}	stress tensor term (contour integrals)
u_{ij}	displacement tensor
V^{FLD}	load line displacement
V^{CMOD}	crack mouth opening displacement
$\dot{V}^{FLD}, \dot{V}_C$	load line displacement rate
W	width of CT specimen, width of weld (X-weld)
$\dot{W}$	strain energy density $(\dot{\varepsilon})$

Greek letters

α	multi-axiality constant
$\dot{\Delta}_C$	load line displacement rate
ε_{ij}	strain tensor, failure strain
ε_f	failure strain
ε_o	Ramberg-Osgood constant
ε_{eq}^c	equivalent creep strain
$\dot{\varepsilon}_{ij}^c$	creep strain rate
$\dot{\varepsilon}_c^{cr}$	creep strain rate - columnar zone
$\dot{\varepsilon}_e^{cr}$	creep strain rate - equiaxed zone
$\dot{\varepsilon}_{ref}$	reference creep strain rate
$\dot{\varepsilon}_x$	axial strain rate
$\dot{\varepsilon}_{eq}$	equivalent strain rate
E_{ij}, Σ_{ij}	geometrical distributions of stress/strain (HRR fields)
$\boldsymbol{\eta}, \boldsymbol{\eta}^{LLD}$	calibration factor - C*-integral
$\boldsymbol{\eta}_w$	adjusted calibration factor
θ	angle
Ω	atomic volume
ρ	biaxial loading ratio (longitudinal and transverse)
σ	stress
σ_0	Ramberg-Osgood constant
σ_y	yield stress
σ_{nom}	nominal stress
σ_L	longitudinal stress
σ_{T2}	transverse stress
σ_{eff}	effective stress
σ_r	rupture stress
σ_1	principle stress
σ_{eq}	equivalent stress
σ_r	radial, hoop and axial stress
σ_θ	hoop stress
σ_z	axial stress
$\sigma_{ij}, \sigma_{xx,yy,zz}$	stress tensor, normal stresses
$\tau_{r\theta}$	shear stress
φ	damage constant
X	material hardening variable (damage models)
ω	damage parameter
$\dot{\omega}, \dot{\omega}_c, \dot{\omega}_e$	damage rate, damage rate - columnar and equiaxed regions

Introduction

Many components in power plants and aeroengines, and materials in manufacturing processes undergo temperatures high enough for creep to occur. Components which fall into this category include pipes, pipe bends, turbine blades, nozzle guide vanes, etc. Many of these components are manufactured with welds (see Figure 1) in them and these are regions where failure often occurs.

Two specimen types, namely the cross-weld (CW) and the compact tension (CT) specimens (see Figures 2 and 3) are commonly used to quantify the effects of welds on the creep and creep fracture behaviour of multi-material components. The CW specimen is used to assess the effect of the compound material specimen in a range of orientations. The CT specimen is used to relate the creep crack growth rate to the crack tip material conditions. This paper describes the use of CW and CT specimen types in predicting the creep behaviour in the vicinity of welds and the parameters specific to a specimen type. CW and CT specimens can be removed from components such as welded pipes taking into account the weld orientation (e.g. seam welds, circumferential welds, narrow gap welds, multi-pass welds), size of weld, and the operating stress field within the component itself (e.g. hoop, radial and axial stresses in an internally pressurised pipe or pressure vessel).
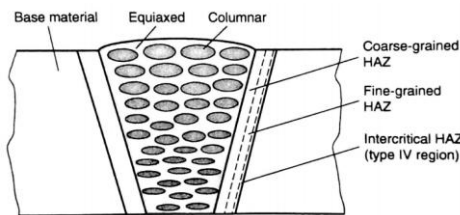

Figure 1. Schematic diagram of a welded joint indicating the three different regions - base or parent material (PM), weld material (WM) and heat affected zone (HAZ).[1]

Within the weld zone cracks can propagate in several regions and may lead to accelerated failures, with the most critical being Type IV cracks (see Figures 4 and 5).[1] Mathematical models have been developed in order to quantify the creep behaviour and creep fracture of welds and cracks present within them (e.g. the Liu/Murakami damage model and the C*-contour integral) and these models are widely used in conjunction with experimental test data from cross-weld and CT specimens. These have been found to provide useful parameters and data for the characterisation of such structural behaviour.[2,3,4] On the face of it, the specimen geometries (cross weld and CT) and simple loading conditions indicate that the stress states within the components during testing are simple. However, the stress states are quite complex and these require careful consideration when interpreting the data obtained from such tests.
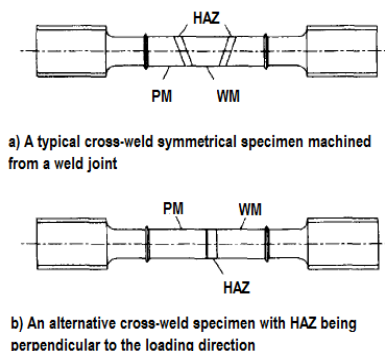

Figure 2. Schematic diagram of a) symmetrical and b) perpendicular typical cross-weld specimens.[5]
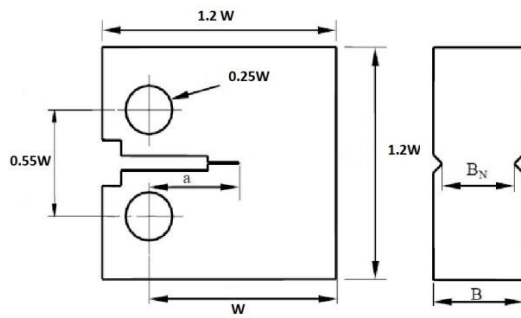
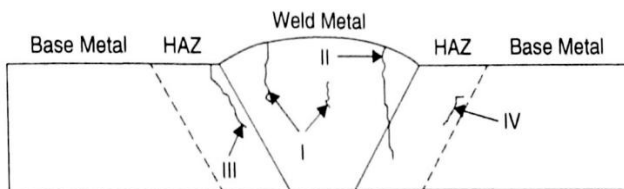**Figure 3.** Schematic representation of a compact tension CT specimen with crack length, a.[1]

Figure 4. Schematic representation of the four different type of cracks within a weld and their typical position.[6]
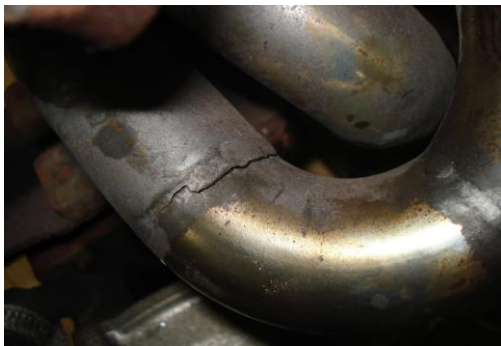

Figure 5. Crack in a pipe weld [courtesy of AMForum].

The present study gives an overview of the usual specimen orientations and analytical procedures, comments on typical results obtained from experimental testing and analysis and indicates potential sources of error. Section Cross-weld specimens deals with the examination of data, modelling and experimental procedures related to the use of cross-weld specimens and Section Compact tension specimen identifies procedures and considerations that should be made when dealing with compact tension specimens.

Structure of Multi-pass welds

The metallurgical structure of a multi-pass weld is complex. Take, for example, the case of a multi-pass circumferential weld in a pipe.[6,7] Each successive bead that is laid down introduces a molten zone from the welding rod. This causes some of the material from previously applied beads to be molten. As these beads solidify, the various regions solidify at different rates resulting in zones of columnar material and zones of equiaxed material.[2] In addition, the temperature-time cycle through which the various regions of the parent material next to the weld metal produces a heat-affected zone (HAZ). Schematic diagrams showing the parent material (PM), weld material (WM) and heat-affected zones are presented in Figures 2 and 4. A photograph of a typical weld structure is shown in Figure 5. The regions of columnar and equiaxed materials and the coarse-grained and fine-grained HAZ zones (see Figure 1) produce a heterogeneous material.

Failure modes in Multi-pass welds

Inspection of welds which have failed or welds which have been taken out of service a number of distinct failure modes can be identified.[2,5,8] The various failure modes are shown in Figure 4 and these are designated Type I, Type II, Type III and Type IV. Type IV cracks are usually regarded as being caused by creep behaviour.

Cross-weld specimens are removed from a weld, as indicated in Figure 6. They are usually produced so that the HAZ is either symmetric or so that the HAZ is perpendicular to the specimen axis (Figure 2). Weld metal specimens are often machined from a weld in the longitudinal or transverse directions as indicated in Figure 7. These are not cross-weld specimens because they contain weld metal only and the specimens are called longitudinal weld specimens or transverse weld metal specimens; these specimens are used to established whether the weld metal material exhibits bulk anisotropy.[2,9,10]
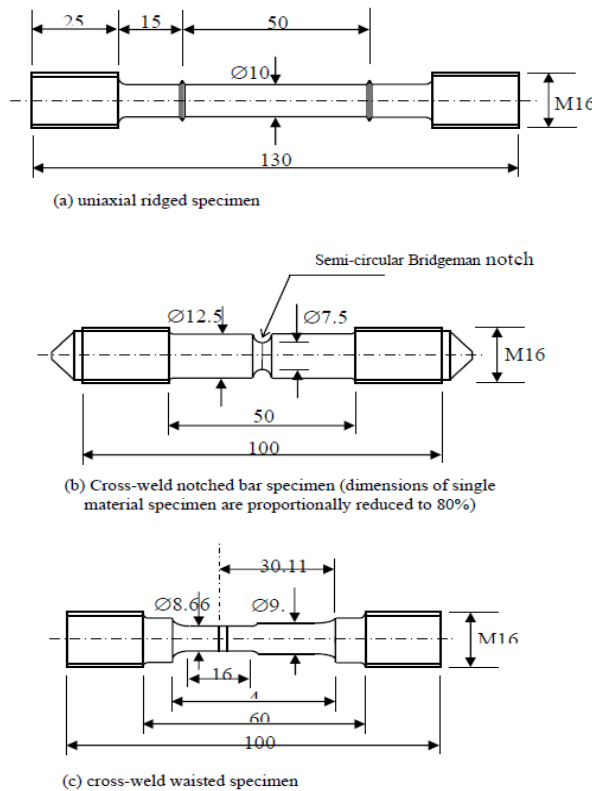

Figure 6. Dimensions of standardised cross-weld specimens - a) uniaxial, b) cross-weld notched and c) cross-weld waisted specimens (all dimensions in mm).[10]

Figure 7. Schematic representation of the microstructural orientation within a typical weld.[11]

Cross-weld specimens

Specimen extraction, geometry orientation and typical analysis

Figure 7 shows a schematic diagram of a multi-pass weld. The longitudinal direction is the welding direction and for a circumferential weld in a pipe the longitudinal direction coincides with the hoop direction whereas for a seam weld in a pipe,[12] the longitudinal coincides with the axial direction of the pipe (see Figure 8). Depending on the orientation of the weld specimen removed from the welded component (e.g. a pipe joint), the geometry can be defined by the diameter, d, HAZ thickness, t, and the inclination of the
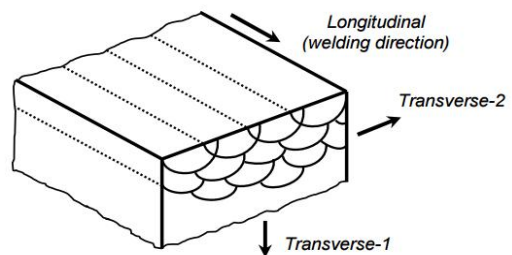
HAZ region, θ. Cross-weld specimens are widely used to describe the bulk creep behaviour and creep failure of welded joints. It is believed that these specimens are able to induce Type IV cracking (see Figure 4) and hence can produce an accurate representation of the failure of welds.[13] This is due to the fact that cross-weld specimens generally include all three material zones - parent material (PM), weld material (WM) and the heat affected zone (HAZ). Creep data extracted from cross-weld specimens is compared to that obtained for PM in order to indicate the effect of the weld on a mechanical structure (e.g. power plant pipes).[1,8]
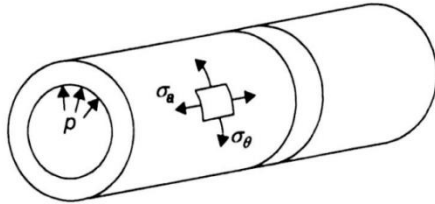

Figure 8. Schematic representation of a circumferential weld in a pipe and corresponding stress field.[14]

Since the weldment comprises of three different material zones three different creep responses are identified due to differences in creep properties (see Table 1) of the materials,[9,10] as indicated in Figures 9 and 10. A standard cross-weld specimen will be of circular cross-section with a diameter of 10 mm with threaded ends, attached to a UTM (Universal Testing Machine), uniaxially loaded along the axis of the bar.[10] Variants of uniaxial cross-weld specimen exist such as the waisted and the notched cross-weld specimens (indicated in Figure 6) with differences in the creep behaviour obtained from the two (see Figure 10). Typical experimental data is shown in Figures 10 and 11 for P91 steel at 625°C. Cross-weld specimen testing is also used to verify that Type IV cracks, initiated in the fine-grained region of the HAZ, are the most common within a weld since smaller grain sizes indicate more grain boundaries present,[8] and hence provide fast diffusion paths, thus leading to void formation and crack initiation (see Appendix 1).[15]
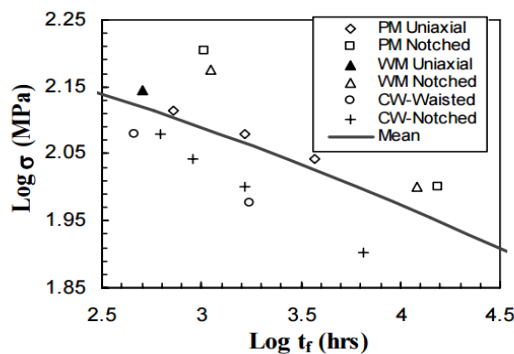

Figure 9. Creep rupture data obtained from parent material, weld metal and cross-weld creep rupture tests at 625°C, compared with the P91 mean data.[10]

Table 1. Creep rupture life and MSR for PM and WM (P91 weld) at 625°C for σ_{nom} = 120 MPa.[10]

Material	Creep rupture life /h	Minimum strain rate /h^{-1}
PM (P91)	1657	2.185×10^{-5}
WM (Chromo 9V)	>1700	6.022×10^{-6}

The weld angle orientation varies for different specimens - e.g. symmetrical cross-weld and cross-weld with perpendicular heat affected zone (see Figure 2) - depending on their

extraction orientation and weld direction leading to changes in the creep life data, as shown by Tanner et al.[16] This aspect of cross-weld specimen testing is covered further in this study. Creep rupture lives and creep strains are usually extracted from cross-weld specimen experimental testing, providing data which is applicable to creep life estimations of welded internally pressurized pipes.[2] Since a large number of weld types exist (e.g. circumferential, seam, etc.) difficulties arise in the selection of specimen extraction orientation which is dictated by the behaviour of the microstructural developments within WM zone and the orientation and size of the HAZ.[9]
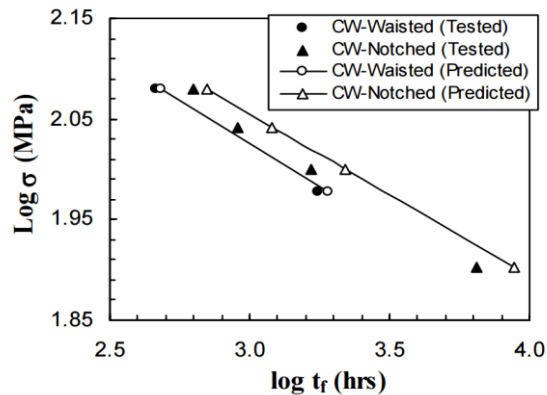

Figure 10. Creep rupture lives of cross-weld waisted and notched bar specimens at 625°C, predicted using the material properties generated, compared with experimental data for P91.[10]
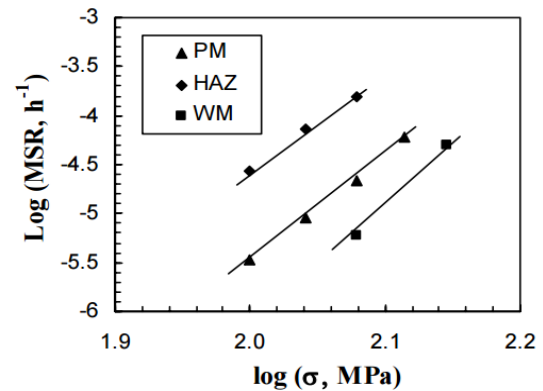

Figure 11. Minimum creep strain rate data of parent material, weld metal and HAZ at 625°C, obtained from uniaxial tests of P91.[10]

Consideration of stress field and weld material orientation

Power plant pipes are thick and the corresponding stress field comprises of three stresses - radial σ_r, hoop σ_θ and axial σ_a. Usually, for experimental testing and FE creep predictions of cross-weld specimen behaviour only axial and hoop stresses are considered. Axial stresses are considered as predominant over hoop stresses since the total axial stress includes effects of the internal pressure in the pipe and the bending stresses,[11,17] arising from the length and weight of the pipe itself. Consideration should be made of the significance of hoop stresses arising in the structures - in shorter pipes the axial stress distribution will be less than the hoop stress, thus the stress field should be selected accordingly.[1] Axial and hoop stress field orientation, with respect to the weld geometry, is also critical - for circumferential welds the hoop stress orientation will coincide with the weld longitudinal direction (see Figure 7) whether in a seam weld hoop stress direction is aligned with the weld transverse direction (see later).

Selection of the stress field and weld extraction orientations should be carefully done with regards to the weld material zone. Within the weld material a three-directional anisotropy is present as a result of the microstructural developments within the material. Equiaxed and columnar regions (see Figure 12) exist within the weld material and loads applied in different directions will produce distinct creep behaviour with different material properties are associated with the two regions (see Table 2). The anisotropy of the weld material is represented in a three-dimensional coordinate system -

longitudinal (Longi), transverse-1 (Trans-1) and transverse-2 (Trans-2) directions. The longitudinal direction coincides with the weld direction and the transverse-2 direction is aligned perpendicularly. Thus in circumferential welds the Longi-direction will be orientated in the hoop stress direction with the Trans-2 aligned with the axial stress direction.[2,18]
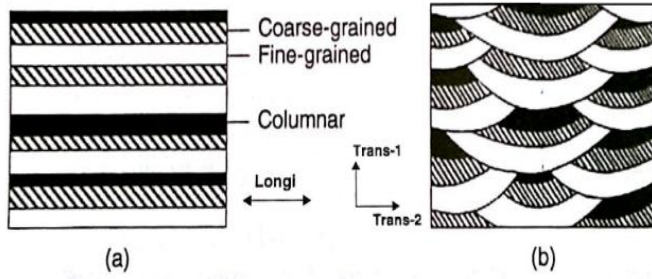
Figure 12. Illustration of microstructural developments in a) longitudinal and b) transverse directions within a weld.[2]

Table 2. Material properties in damage equations used to describe anisotropic behaviour of WM (columnar and equiaxed) of 9CrMoNbV at 650°C.[14]

Material	A	n	B	φ	χ	α
Equiax.	1.37×10^{-20}	7.65	1.6×10^{-20}	11.46	7.95	0.59
Column.	2.74×10^{-21}	7.65	3.2×10^{-21}	11.46	7.95	0.59

Weld pads and specimens removed from them are typically used to describe the difference between the creep behaviour of WM zone when an uniaxial load is applied along either Longi or Trans-2 directions. From Figure 13 it can be noted that loading applied in the longitudinal direction results in higher creep strength than a corresponding loading in the transverse direction. This phenomenon arises due to the difference in crack paths which naturally exist within the microstructure, since along the longitudinal direction extension of cracks is possible along the length of the specimen resulting in load redistribution from the columnar to the equiaxed regions, thus increase in creep strength.[2]
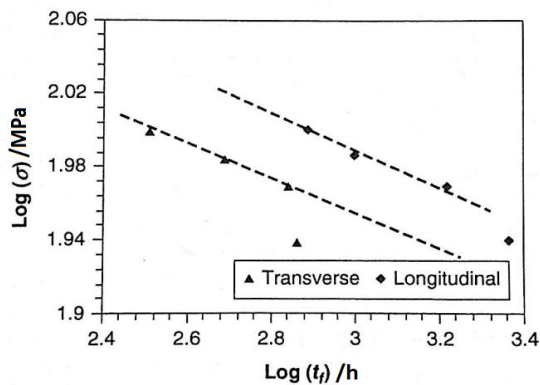

Figure 13. Uniaxial stress vs. rupture time for 9CrMoNbV weld metal at 650°C. The difference in stress states between the two orientations are clearly observed.[2]

The unit cell model method was used by Hyde et al.[14] to represent the columnar and equiaxed regions within the weld (see Figure 14) via a damage-based approach, using either Kachanov[19] - equations (1) to (3) - or Liu/Murakami method[20] - equations (4) to (6).

$$\dot{\varepsilon}_{ij}^c = \frac{3}{2} A \left(\frac{\sigma_{eq}}{1-\omega} \right)^n \frac{S_{ij}}{\sigma_{eq}} t^m \qquad (1)$$

Where the damage rate in the Kachanov model is:

$$\dot{\omega} = B \frac{\sigma_r^\chi}{(1-\omega)^\varphi} \tag{2}$$

$$\sigma_r = \alpha\sigma_1 + (1-\alpha)\sigma_{eq} \tag{3}$$

The multi-axial form of the Liu/Murakami method being:

$$\dot{\varepsilon}_{ij}^c = \frac{3}{2} C \sigma_{eq}^{n2} \frac{S_{ij}}{\sigma_{eq}} \exp \frac{2(n_2+1)}{\pi \sqrt{1+\frac{3}{n_2}}} \cdot \left(\frac{\sigma_1}{\sigma_{eq}}\right) \cdot \omega^{\frac{3}{2}} \tag{4}$$

where the damage rate in the Liu/Murakami model is:

$$\dot{\omega} = D \frac{1-e^{-q_1}}{q_2} \sigma_r^p \, e^{q_2\omega} \tag{5}$$

$$\sigma_r = \alpha\sigma_1 + (1-\alpha)\sigma_{eq} \tag{6}$$

It should be noted that the damage parameter, ω, in the creep rate expression - equation (4) - is time-dependent and this is can be shown by integrating the damage rate expression, equation (5) (see Appendix 2).

The resultant damage contours showed that for both Trans-1 and Trans-2 directions failure takes place within the equiaxed region, diagonally to the columnar zones. In contrast to this phenomenon, load applied along the longitudinal (Longi-z) will result in damage within the columnar region boundaries.[14]
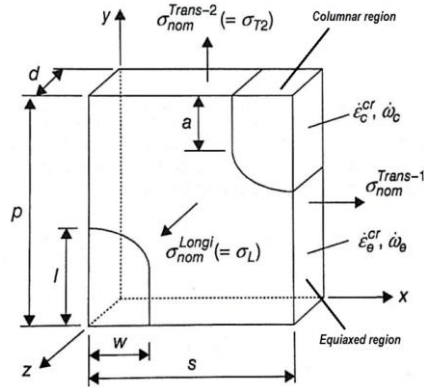

Figure 14. Schematic diagram of the unit cell model used to describe variation of creep strain for longitudinal, transverse-1 and transverse-2 directions.[14]

Thus loading of a cross-weld specimen along the longitudinal direction, e.g. hoop stress considered in a circumferential weld or axial stress in a seam weld, will result in longer creep life and high creep-ductile behaviour, as indicated in Figure 15. In contrast, when the load applied coincides with the transverse direction, i.e. axial stress in a circumferential weld or hoop stress in a seam weld, shorter creep life and higher bulk creep strains are to be observed, indicating more creep-brittle behaviour.[2]
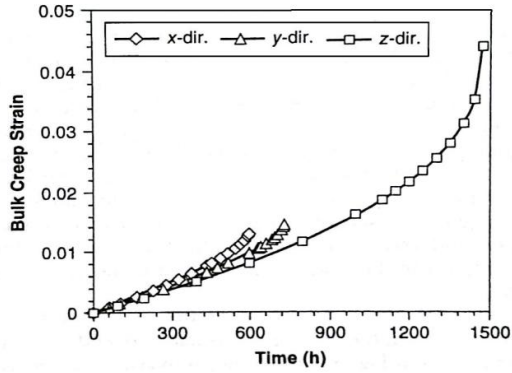
Figure 15. Variation of bulk creep strain with time obtained via damage analysis for σ_{nom} for the three loading directions.[14]

Assuming that the stress state of the system is biaxial, the ratios of the load applied in longitudinal and transverse direction is:

$$\rho = \frac{\sigma_L}{\sigma_{T2}} \tag{7}$$

where σ_L is the stress in Longi-direction and σ_{T2} - in the transverse.[11] Following from this, the failure behaviour and stress states within the unit cell under biaxial loading will be dictated by the material properties, biaxial stress ratio, ρ, and the triaxiality parameter, α, see equations (1) to (6). The highest failure life is observed to occur at $\rho=2$ and respectively, the lowest at $\rho=-1$, where θ in Figure 16 is used to represent biaxial loading ratio in the following form:

$$\theta = \tan^{-1}(\rho) \tag{8}$$

From the above statement, a consideration is made such that failure in a biaxial real life condition is controlled by the transverse direction bulk properties since they are weaker than the longitudinal, agreeing with Hyde et al.[11]
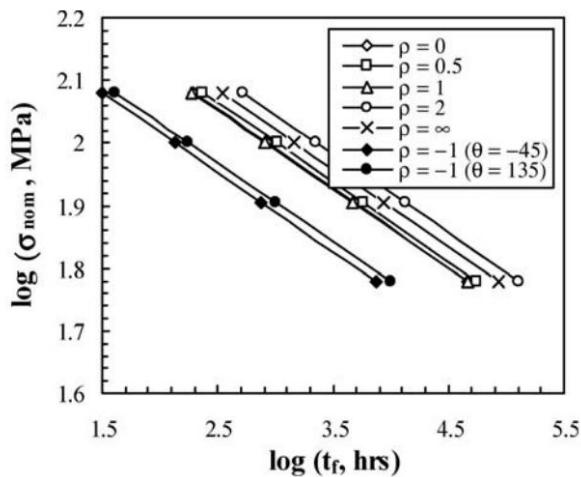

Figure 16. Variations of failure life with nominal stress for different biaxial loading conditions, $\rho = \sigma_L/\sigma_{T2}$, obtained via damage analysis.[11]

Consideration of material properties mismatch and weld dimensions

In order to examine the effects of material properties and weld dimensions on the creep behaviour of a cross-weld specimens, simplified analysis of a two material cross-weld specimen geometry with the centre-line at r=0 (see Figure 17) was conducted by Hyde et

al.[8,21] For the sake of simplicity both materials A and B obey the Norton power law creep as indicated in equation (9).

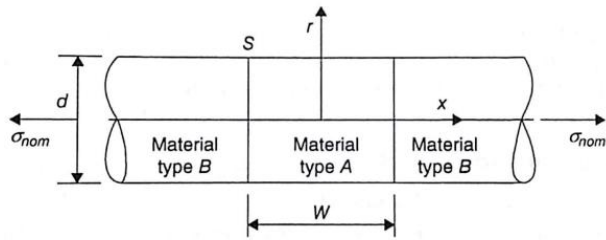$$\dot{\varepsilon}_{A,B} = C\sigma^n \ where \ C = (A,B) \tag{9}$$

Figure 17. Schematic diagram of a two material idealised cross-weld specimen.[5]

By observing Figure 18 the variation of the normalised axial stresses with the creep exponent, n, is continuous whether discontinuities are present in the variation of the normalised equivalent stress, σ_{eq}/σ_{nom}, at the A/B material boundary. It should be noted that discontinuities will be larger for smaller n-values and thus care should be taken, agreeing with Hyde et al.[8]
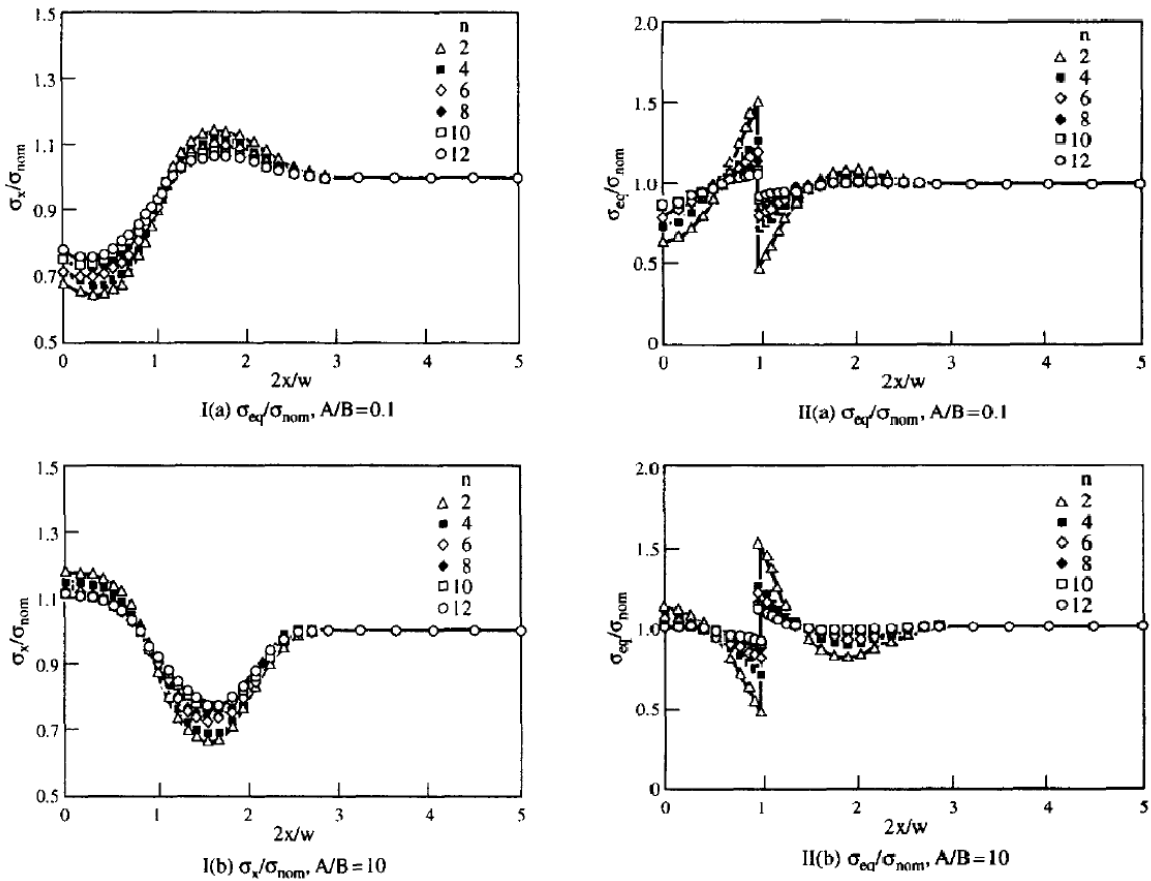

Figure 18. Effect of n at the centre-line variation of the axial and equivalent normalised stresses for different 2x/w ratios (positions) (N.B. w/d=1, A/B=0.1 and 10).[5]

From compatibility and equilibrium at the centre-line (r=0) the following relations are obtained:

$$\sigma_r = \sigma_\theta \tag{10}$$

$$\sigma_{eq} = \sigma_x - \sigma_r \tag{11}$$

$$\dot{\varepsilon}_x = \dot{\varepsilon}_{eq} \tag{12}$$

$$\dot{\varepsilon}_r = \dot{\varepsilon}_\theta = -\frac{\dot{\varepsilon}_x}{2} = -\frac{\dot{\varepsilon}_{eq}}{2} \tag{13}$$

Large discontinuities in the normalised equivalent stress are also present for varying A/B ratios. The maximum value of the normalised axial stress occurs at the centre of material A for A/B>1 whether the equivalent normalised stress peaks at the A/B interface for A/B<1 (see Figure 19). An important consideration should be made on the variation of σ_x/σ_{nom} within both materials with w/d and log(A/B). Clearly, the maximum values of the normalised axial stresses within material A are governed by w/d and vary significantly. In comparison, these values are less dependent on w/d for material B (see Figure 20).
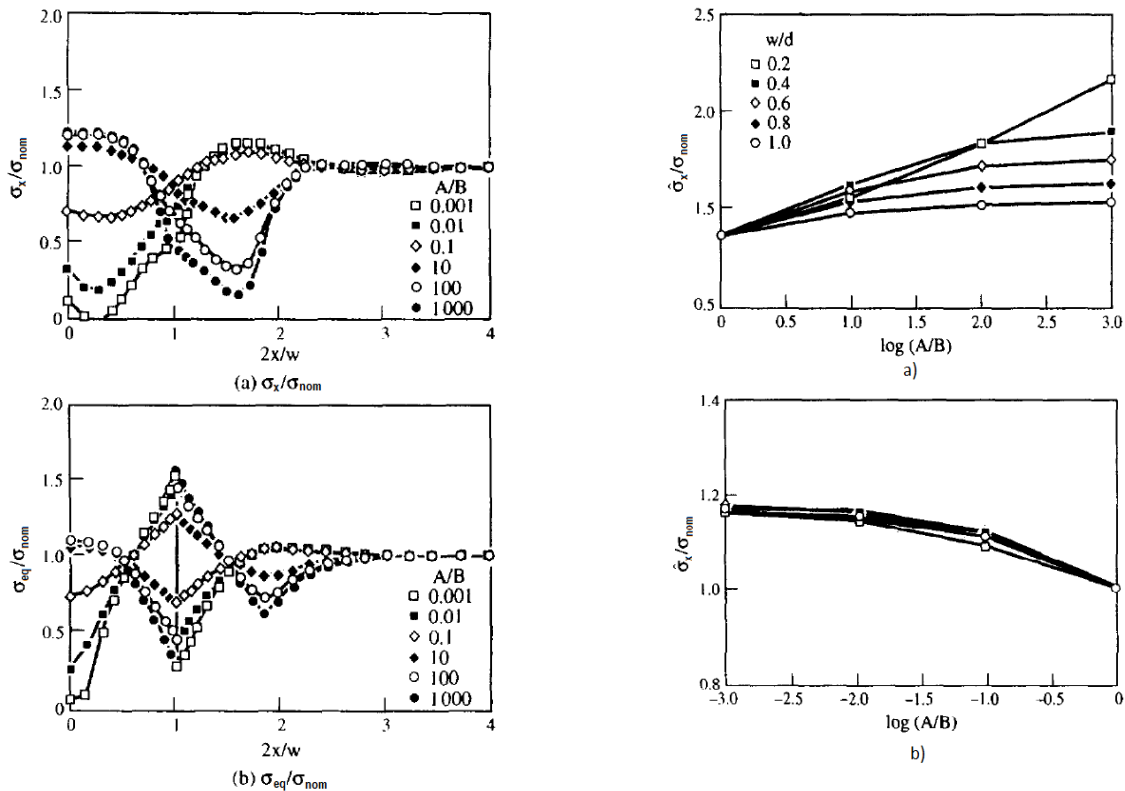

(a) σ_x/σ_{nom}

(b) σ_{eq}/σ_{nom}

Figure 19. Effect of A/B ratio at centre-line variations of the normalised stresses (a) axial and b) equivalent with 2x/d for w/d=1 and n=4.[5]
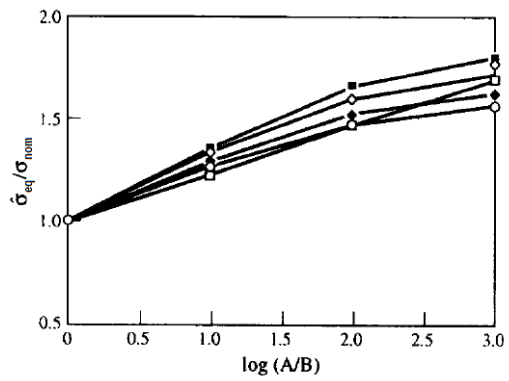

a)

b)

Figure 20. Effects of w/d on the centre-line variations of axial normalised stresses with log(A/B) for n=4: a) Material A at A/B>1 and b) Material B at A/B<1.[5]

The peak values of the normalised equivalent stresses with different w/d ratios occur at the same positions as the axial stress values, but large stresses in material A at the interface are observed for A/B<1 and in material B for A/B>1, again at the mismatch interface (see Figure 21).

Variations with w/d within the materials at the centre-line of the normalised equivalent stresses are significant with discontinuities at the interfaces (see Figure 22). Normalised axial stress peaks in material A for A/B>1 and in material B for A/B<1. Contrary σ_{eq}/σ_{nom} peaks at interface for material A and away from it for material B when A/B<1 and at the centre of material A and interface of material B for A/B>1 (see Figure 22). These observations lead to an important design consideration - reduction in the equivalent stress is observed,[5] when material A is less creep resistant than material B, following the model geometry and material configuration demonstrated in Figure 17.
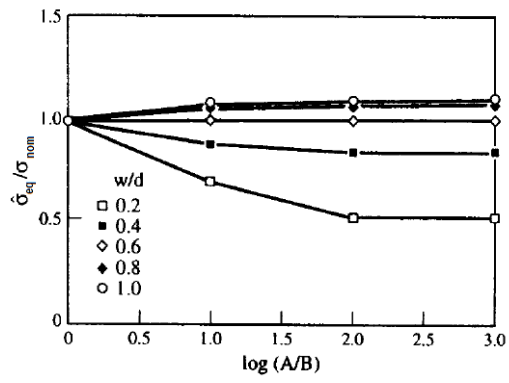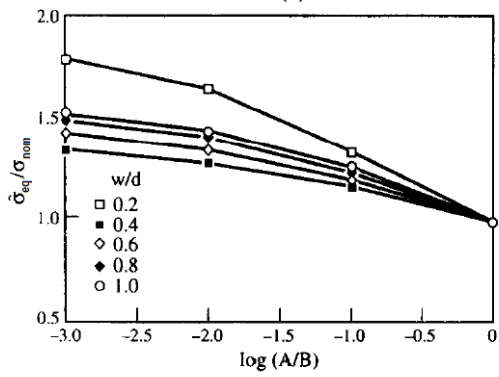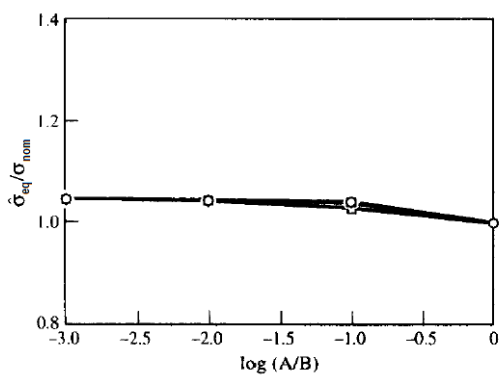
Figure 21. Effects of w/d on the centre-line variations of equivalent stresses with log(A/B) for n=4: a) Material A at A/B>1 and b) Material B at A/B<1.[5]

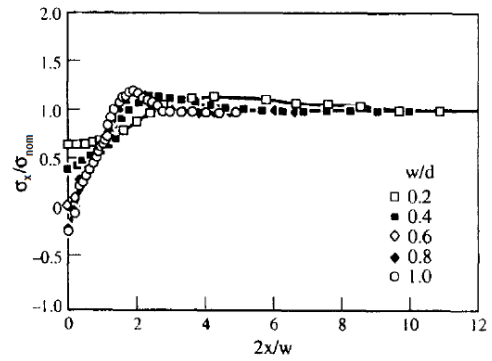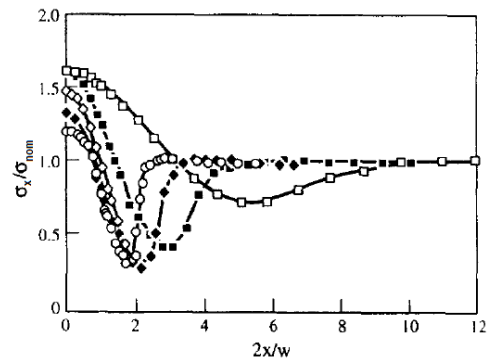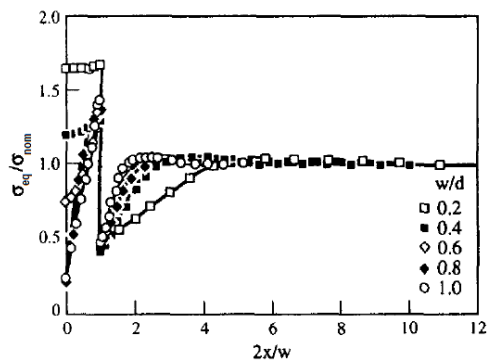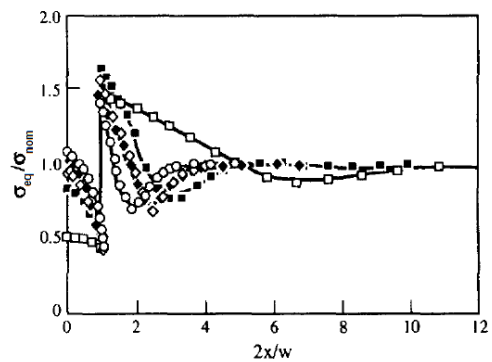**Figure 22.** Effect of w/d on the centre-line variations of axial and equivalent normalised stresses with 2x/w for n=4 and A/B=0.01 and 100.[5]

Consideration of stress singularity, weld angle and damage behaviour

A stress singularity is present at the free surface of two distinct material cross-weld specimen with different properties under steady-state creep conditions, as described by Hyde et al.[1] In order to describe the singularity arising in a cross-weld specimen the same idealised geometry and configuration (Figure 17) of the component is used with a polar coordinate system being adopted to describe the distinct stress singularity states (see Figure 23).

It is observed that a large increase in stress is present as r→0 and thus the normalised stress states are suggested to take the form of the following expressions,[21] where N_{ij} and N_{eq} represent exponent terms and K_{ij} and K_{eq} characterise the variation of stress with angular orientation, θ:

$$\frac{\sigma_{ij}}{\sigma_{nom}} = K_{ij} \left(\frac{r}{d}\right)^{-N_{ij}} \tag{14}$$

$$\frac{\sigma_{eq}}{\sigma_{nom}} = K_{eq} \left(\frac{r}{d}\right)^{-N_{eq}} \tag{15}$$

The variations of the singularity exponents with different value of the creep exponent, n, are negligible, thus the stress singularity is weakly dependent on n-values (see Figure 24). On the other hand, N_{ij} and N_{eq} vary significantly for different A/B ratios, thus making the singularity exponents strongly dependent on A/B (Figure 25).
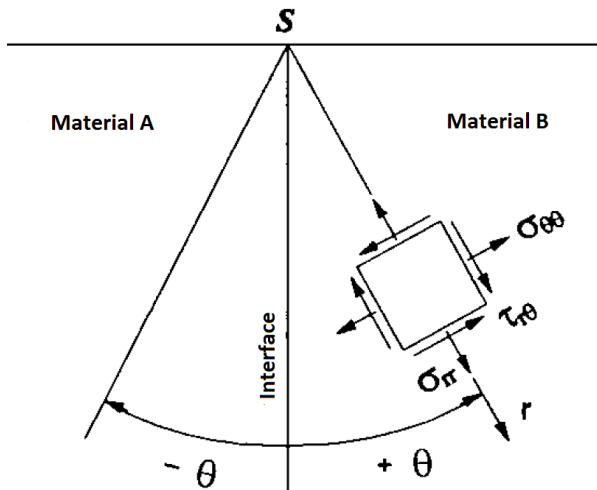

Figure 23. Coordinate and stress component definitions within an idealised cross-weld specimen.[21]
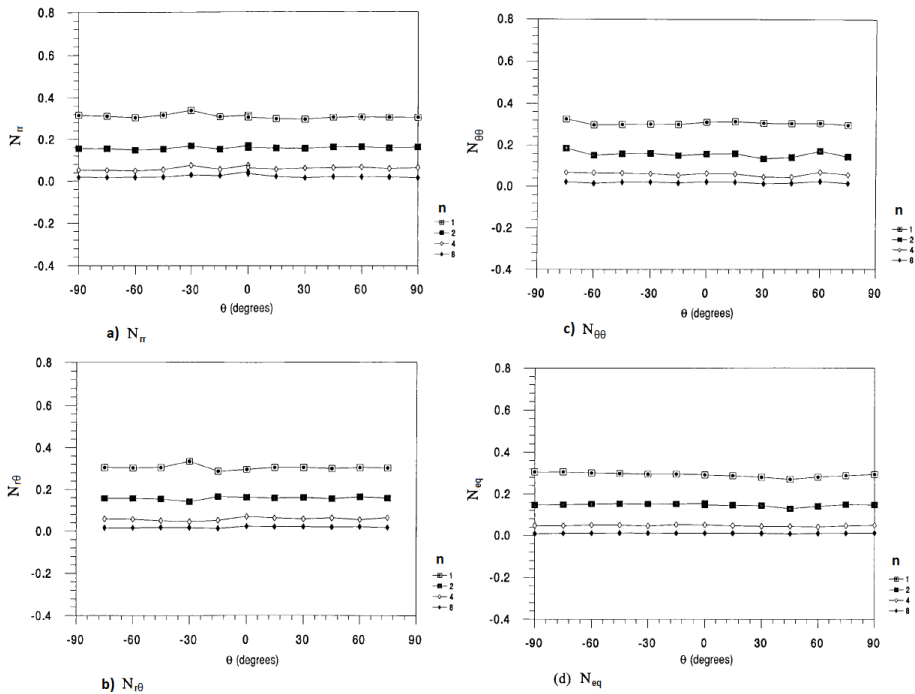
Figure 24. Variation of the singularity exponents N_{ij} and N_{eq} within the polar coordinate system, θ, for a range of n-values (N.B. w/d=1 and A/B=0.1).[21]
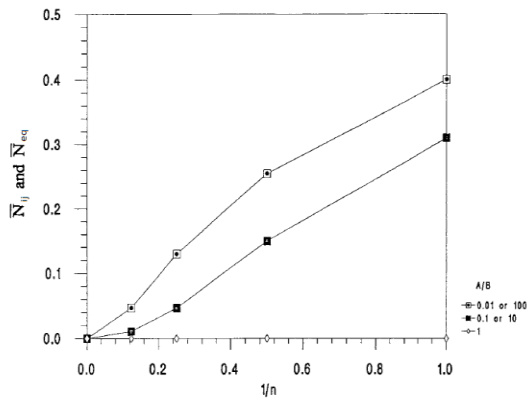

Figure 25. Varying averaged values of N_{ij} and N_{eq} with 1/n for different A/B ratios, w/d=1.[21]

The behaviour of the K-functions is more complex since they represent the variation of the stress in terms of the coordinate system. Large discontinuities in the variation of K_{rr} and K_{eq} are present at the position of the interface ($\theta=0°$) for different values of creep exponent, n, whether the other two K-functions appear to be continuous, as shown in Figure 26. The data indicates that K_{ij} and K_{eq} are strongly dependent on the creep stress exponent, n,[21] and will vary significantly from one material to another for high n-values (n≈8).

K_{ij} and K_{eq} also depend on the values of A/B significantly and care should be taken when identifying the maximum values.[1] The values of K_{rr} peak at the surface of material A for A/B<1 and at surface of material B for A/B>1. $K_{\theta\theta}$ reaches a maximum in material A ($\theta≈15°$) for A/B>1 and within material B zone for A/B<1. Peak $K_{r\theta}$ values are observed in material A for A/B<1 and in material B for A/B>1 (same behaviour as K_{rr} and K_{eq}), agreeing with observations from Hyde et al.[21]

Variations of K_{eq} values with respect to w/d positions are examined and it should be noted that results for w/d=0.5 and 1 are practically the same with the singularity at one interface being not affected by another interface in a remote field (see Figure 27). But for w/d=0.1 the data indicates that interactions between the two singularities occur, invalidating the singularity expressions - equations (14) and (15).

(a) K_{rr}

(b) $K_{\theta\theta}$

(c) $K_{r\theta}$

(d) K_{eq}
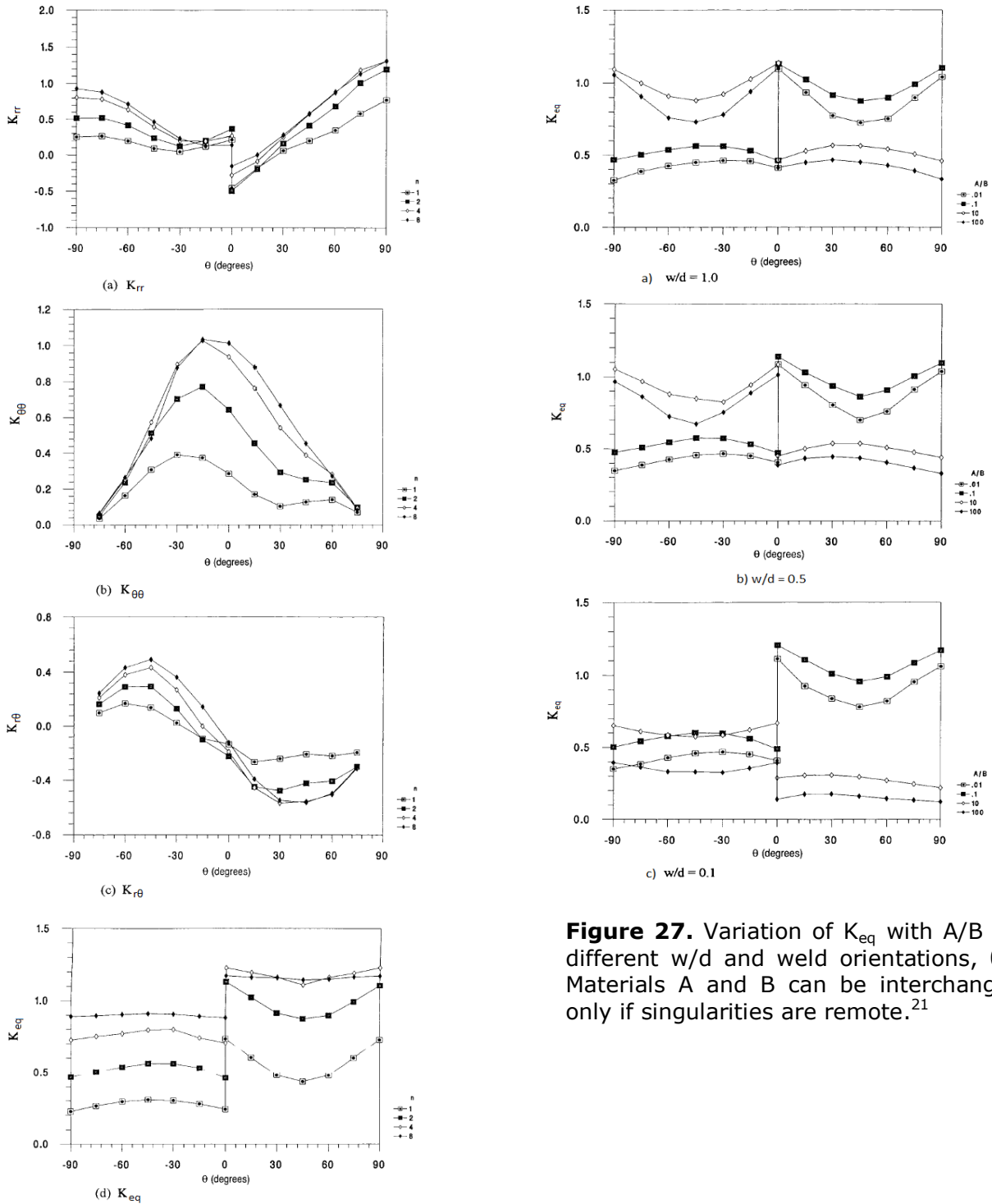
Figure 26. Varying K_{ij} and K_{eq} with the stress exponent, n, for a range of angular positions, θ. Discontinuities in K_{rr} and K_{eq} values at 0° are identified.[21]
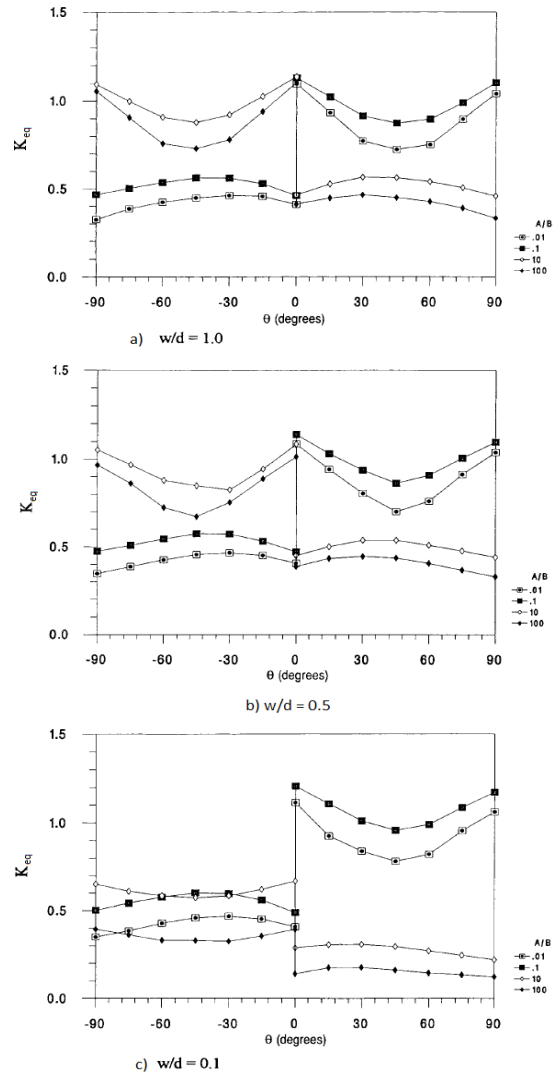
a) w/d = 1.0

b) w/d = 0.5

c) w/d = 0.1

Figure 27. Variation of K_{eq} with A/B for different w/d and weld orientations, θ . Materials A and B can be interchanged only if singularities are remote.[21]

The orientation of the weld angle with respect to the loading axis should also be considered when dealing with cross-weld specimens. Predictions of the creep life variations of a P91 weld, with the constants used shown in Table 3, three material cross-weld specimen (see Figure 28) for a set of different weld angles were conducted via the Kachanov and Liu/Murakami material models, both of them resulting in accurate estimations.[11] The highest creep life (~750 h) is obtained for a weld angle orientated at 90° to the load axis, whether the minimum failure life happens to be for a weld angle between 25° and 30°, with the value being more than a half from the maximum recorded. This the orientation of weld angle with respect to the load axis should be considered when using cross-weld specimen data to characterise pipe welds.[16,22]
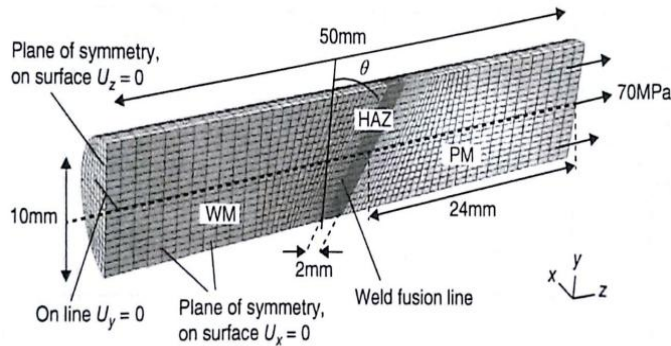

Figure 28. Cross-weld specimen FE model used to determine variation in failure times for different weld angles.[16]

The creep behaviour of a cross-weld specimen within the tertiary creep region can also be modelled with the Kachanov damage model[19] (equations (1) to (3)) providing a suitable level of accuracy, as indicated in Figure 29. It is assumed that the time to achieve high damage levels in a small number of elements along the diameter of the cross-weld specimen is a close approximation to the time to failure for complete damage (ω=1) of the whole specimen.[8]

Different behaviour characteristics of waisted and notched cross-weld specimens were observed. Wasted and notched cross-weld specimens are used to describe the creep damage response of a CrMoV weld at 640°C.[8] Figure 30 shows damage contours obtained for $t/t_f \approx 1$, indicating that highest damage will take place within the fine grained HAZ, clearly indicating the behaviour of a type IV crack failure.[10] A consideration should be made of the maximum damage position in the notched specimen, i.e. at the minimum cross-section, meaning that failure may not always be related to a type IV crack formation. Comparison between the steady-state creep life predictions and the tertiary creep damage model predictions indicate that the stationary state estimations are ~0.60 compared to the damage values, clearly notifying that either Kachanov or Liu/Murakami models should be used for accurate creep rupture life predictions, with the latter being more suitable for notched specimens.[23,24]

Table 3. PM, WM and HAZ L/M damage constants used for P91 weldment at 650°C to describe effect of weld angle.[16]

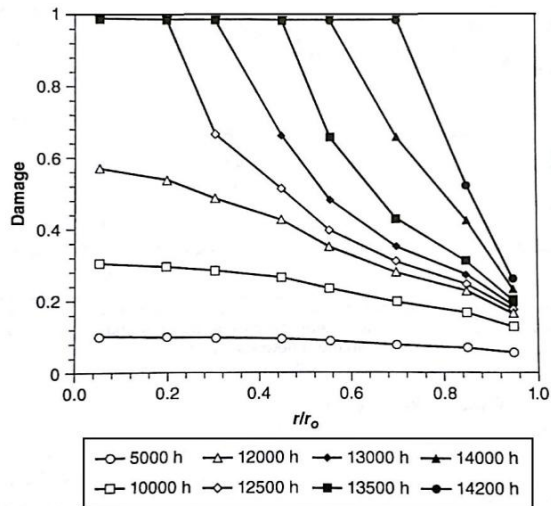| Zone	A	n	m/q²	B	ϕ	χ	α
PM	1.09×10^{-20}	8.462	0/3.2	3.537×10^{-17}	7.346	6.789	0.31
WM	1.37×10^{-20}	7.65	-0.00366/5.0	1.6×10^{-20}	11.463	7.95	0.81
HAZ	2.3×10^{-20}	8.462	0/2.8	1.522×10^{-14}	7.346	5.502	0.52

Figure 29. Damage history in a cross-weld waisted specimen varying with the normalised radial position at the centre-line at σ_{nom} = 25MPa for 1/1Cr/Mo1//4V:2.25Cr1Mo weldment at 640°C.[8]
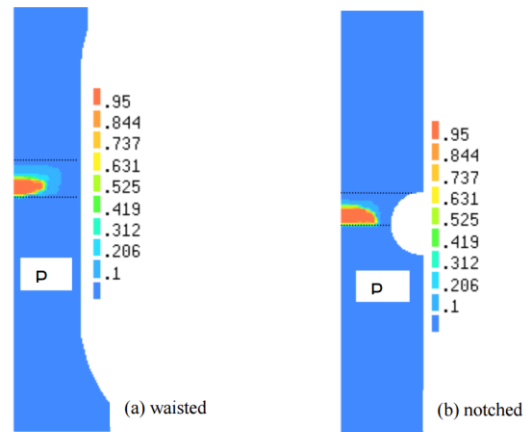

Figure 30. Damage contours at times close to failure for the cross-weld waisted specimens: (a) waisted, at 95MPa, showing HAZ failure near the parent material, and (b) notched, at 100MPa, showing HAZ failure at the minimum notch section.[10]

Large cross-weld specimens, narrow gap welds and multi-pass

Large cross-weld specimens are also being used to assess creep life of pipe weldments. They tend to yield estimations of the creep behaviour closer to the real life conditions, since their size represents more realistically the geometry of the pipe weld (N.B. usually cross-weld specimens are small).[25] Failures associated with type IV cracks are similar to the ones described by small cross-weld specimens, with the effects of the microstructural difference between the WM and HAZ being more significant within the large cross-weld specimen.[25]

Important considerations can be taken into account of the modelling of narrow gap welds as their popularity increases. Comparison is made between a typical V-type weld and a NG weld by Hyde et al.[23] with the difference in the creep life estimates being small (see Figure 31). It is identified that the Liu/Murakami damage model is preferred to the Kachanov model due to the small-scale geometry of the NG weld and the corresponding localised increases in stress.[26]

The effect of different creep properties of the materials on the failure behaviour is also examined and it is determined that varying properties will change only the position of failure, with the time to failure values remaining unchanged, as indicated in Figure 32 (infinitesimally small difference in t_f).
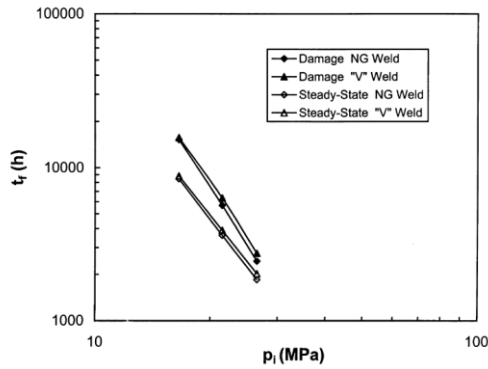
Figure 31. Failure life against internal pressure predicted by damage and steady-state analysis for narrow gap weld (W = 8 mm) and "V" weld.[23]
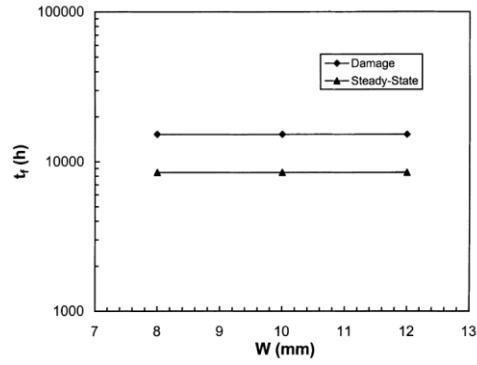

Figure 32. Failure life as a function of weld metal width predicted by damage and steady-state analysis for narrow gap weld (p_i = 16.55 MPa).[23]

Observations on modelling and experimental testing of multi-pass welds via cross-weld specimens and not only leads to conclusions that large residual stresses initiate across the thickness of the weld (see Figure 33) and care should be taken when modelling such structures.[27,28] In some cases, e.g. narrow gap laser and gas tungsten arc multi-pass welds, the difference in the tensile residual stresses across the thickness is 30-40%,[26] which may often result in discrepancies in static and creep behaviour data.
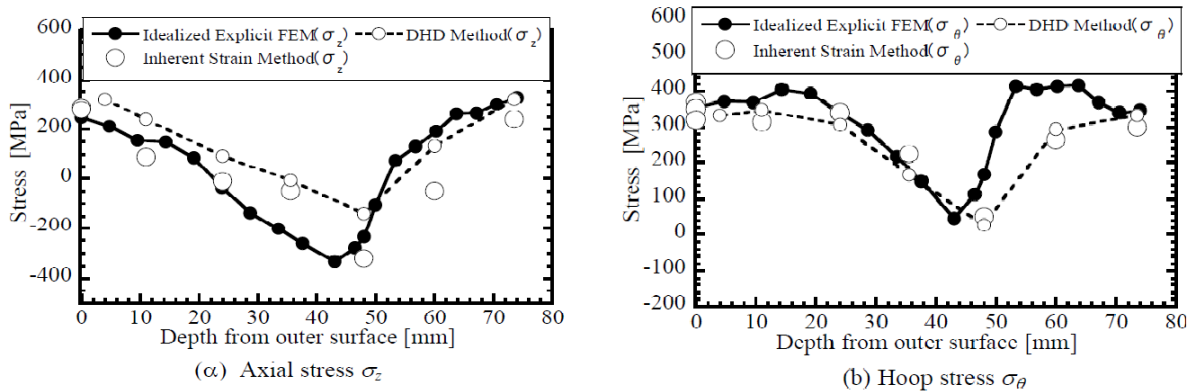

(α) Axial stress σ_z

(b) Hoop stress σ_θ

Figure 33. Variations of a) axial and b) hoop stress through the depth of a multi-pass weld. Residual stresses are identified.[27]

Summary of complications to the use of cross-weld specimen stress state

In this section it has been shown that even for the simple geometry and loading conditions that exist for the CW specimen, the stress and deformation conditions are complicated. The factors which influence the behaviour of such specimens include:

- Material behaviour (either simple Norton creep models or more complex damage mechanics models)
- Unit cell models show that stress discontinuities exist between the columnar zone and equiaxed zones within the weld material
- Stress singularities at the material interfaces on the surface of CW specimens
- Specimens can be obtained by machining in the longitudinal and transverse (relative to welding direction) directions, i.e. the θ-value has a significant effect on the stress distribution produced in a CW specimen
- Residual stresses will affect the variation of stress through the thickness of the weld.

Compact tension specimen

Specimen extraction, geometry orientation and typical results

Compact tension CT specimens are widely used to characterise the creep behaviour of cracks within dissimilar material structures. CT specimens provide a feasible way of representing a crack within weld joints since the position of the crack within the material zones can be adjusted accordingly to the geometry.[29] Typical extraction configurations of the specimen will include a PM CT specimen, PM and WM specimen and a full representation of the across weld material variation featuring PM, WM and HAZ, as shown in Figures 34 and 35.
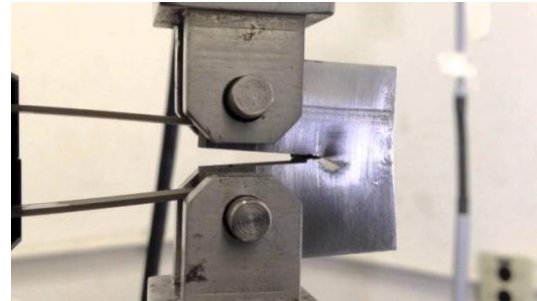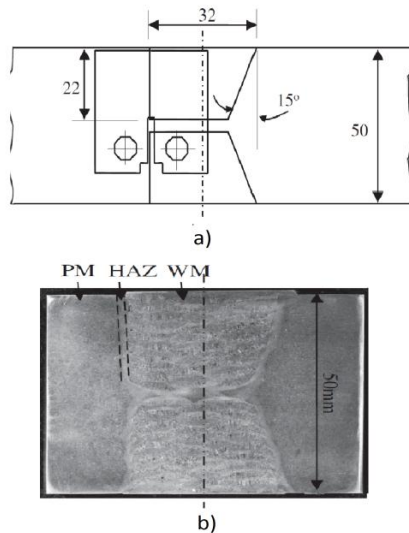

Figure 35. Fracture testing of a CT specimen under uniaxial loading [courtesy of Federal University of Rio de Janeiro].

Figure 34. CT specimen extraction, a), from an etched weld macro-section, b).[4]

The dimensions of the CT specimen follow the ASTM E1457-13 standard and are shown in Figure 36.[30] Using a standardised geometry allows useful parameters and geometrical identities (e.g. crack growth rate $\dot{a}$, load line displacement rate $\dot{V}_c$ and CMOD) to be recorded which can be used to quantify the creep behaviour and failure of welds.[31]

Experimental testing and modelling of a CT specimen is typically based on uniaxial loading of the sample on UTM which results in a Mode I opening crack growth mode of the pre-existent crack.[32] The crack is often positioned within the fine grained HAZ region associated with type IV crack failures termed as the most detrimental, but also other geometry configurations are used depending on the crack type considered (see later).
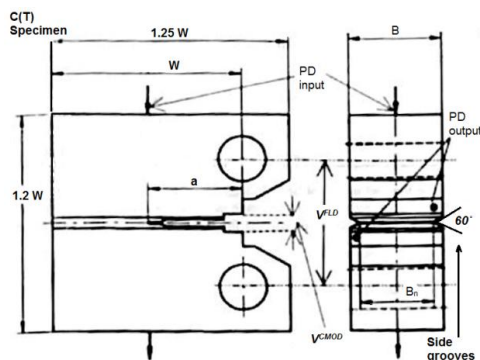

Figure 36. Representation of CT specimen, based on the ASTM E1457 standard. The load line displacement is denoted by V^{FLD} and the crack mouth displacement by V^{CMOD}.[30]

Typical data extracted from experimental testing describing CCG is demonstrated in Figure 37 - load line displacement, V^{FLD}, versus time and crack length versus time respectively - in this cases describing the creep response and time to failure of a P91 weld at 650°C.

Mathematical models describing creep behaviour are widely used in conjunction with the CT specimen geometry resulting in rapid and accurate predictions of the creep failure of internally pressurised welded pipes.

There are two mathematical methods commonly used for predicting creep crack growth rates, as proposed by Hyde et al.[33] and Davies et al.[3] The methods are based on damage mechanics - e.g. the Kachanov model (equations (1) to (3)) and Liu/Murakami model (equations (4) to (6)) and fracture mechanics approach - e.g. C*-contour integral - equations (16) and (17) respectively. From the two damage models the Kachanov expressions are the most widely used due to the fact that less material parameters and material constants are required to be computed, but the Liu/Murakami model provides greater accuracy for the predictions compared to experimental data.
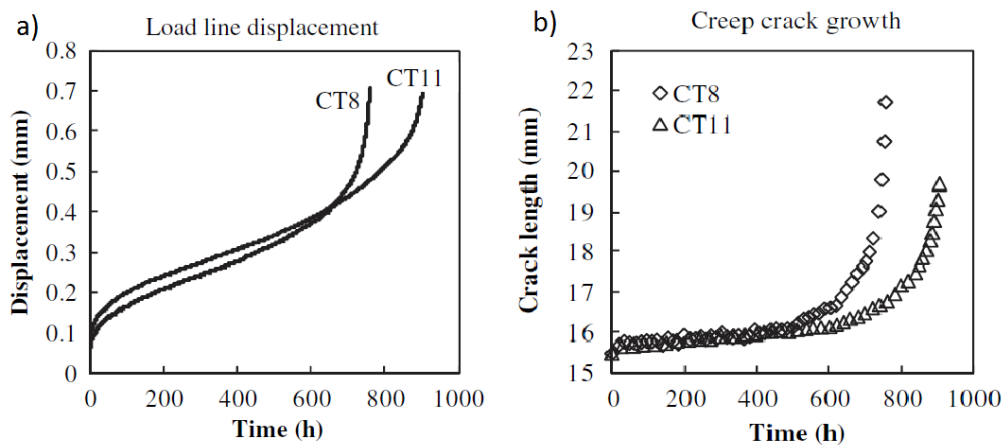

Figure 37. Experimental results of nominally identical CT tests of P91 welds at 650°C - a) displacement vs. time and b) crack length vs. time.[4]

The C*-contour integral fracture parameter is often preferred to the damage mechanics parameters since the C* expression only requires the material constants for Norton power law creep, i.e. n and A (see equations (16) and (17)). This enables rapid computations of time to failure and crack growth rate.[3]

The mathematical form of the C*-contour integral is shown in the following equations (16) and (17), where S is the contour path, surrounding the crack tip (see Appendix 3 and 4):

$$C^* = \int_S \dot{W} dy - T_{ij} \frac{d\dot{u}_{ij}}{dx} dS \tag{16}$$

and

$$\dot{W} = \int_0^{\dot{\varepsilon}_0} \sigma_{ij} d\dot{\varepsilon}_{ij} \tag{17}$$

The C*-integral values are termed to be path-independent, meaning that the value of C* will be same irrespective of the path selected to surround the crack tip (see Figure 38).[15] The integral values are computed either via FE or via empirical formulae (see equations (19) and (20)) based on the ASTM E1457-13 standard.[30] Care should be taken when C*-values are obtained via FE modelling since values differ for plane stress and plane strain

significantly, as described by Nikbin.[34] Several solutions exist with the most widely used being the displacement rate solution related to the load applied, P, and load line displacement rate, $\dot{\Delta}_C$ or $\dot{V}_C$ - equation (18).[31] Relations between the crack growth rate, $\dot{a}$, and C*-integral value can be established and accurate predictions of creep life are obtained (see Figures 39 and 40).
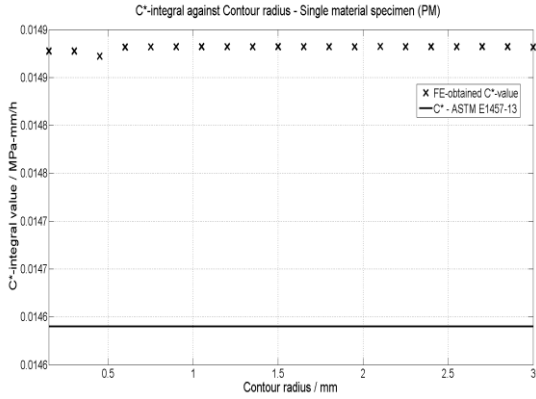
Figure 38. Typical FE and empirical ASTM C*-integral values for different contours surrounding the crack tip in a CT specimen - single material (316 SS PM, homogeneous structure).
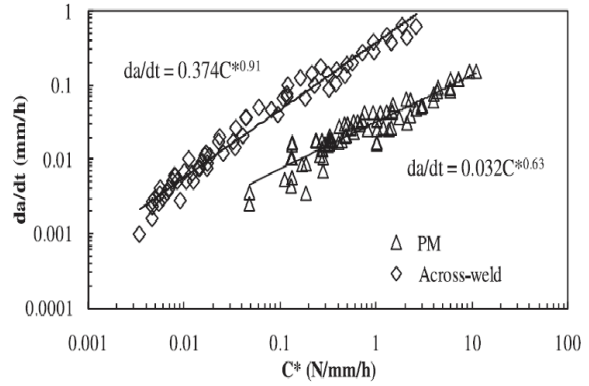
Figure 39. CCG rate vs. C*-integral data obtained from an FE prediction of a P91 PM and cross-weld CT specimen.[4]
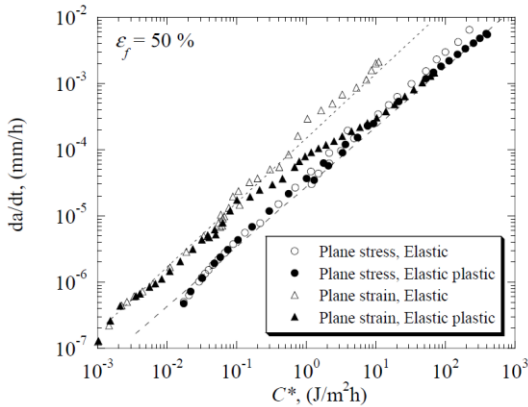
Figure 40. Differences in creep crack growth rate versus C*-integral value for plane stress and plane strain conditions for 316H steel at 550°C obtained via elastic and elastic-plastic FE modelling.[36]

$$C^* = \frac{P\dot{\Delta}_C}{B_N(W-a)} H^{LLD}\eta^{LLD} \tag{18}$$

The expression for C*-integral for a CT specimen geometry with a centre crack and uniaxial loading is:

$$C^* = \frac{n}{n+1}\frac{P\dot{V}_C}{B_n(W-a)}\left(2 + 0.522\left(1-\frac{a}{W}\right)\right) \tag{19}$$

with the relation between the C* and $\dot{a}$, as proposed by Davies et al.[3]:

$$\dot{a} = \frac{(n+1)\dot{\varepsilon}_0}{\hat{\varepsilon}_f}\left(\frac{C^*}{I_n\sigma_0\dot{\varepsilon}_0}\right)^{\frac{n}{n+1}} r_c^{\frac{1}{n}+1} \tag{20.a}$$

Equation 20.a. can be reduced down to the following expression where D and q are material constants, by considering the form of the HRR singularity fields, see equations (22) and (23) around the rack tip,[35] as proposed by Yatomi et al.[36]:

$$\dot{a} = D(C^*)^q \tag{20.b}$$

Considerations of geometry of specimen and residual stresses

Important consideration should be made with regards to the crack growth profile through the thickness of a CT specimen (see Figure 41). The phenomenon of non-uniform growth profiles is described as tunneling and this non-steady crack growth profile is associated with shear stress fields which are present on the side surfaces of the specimen.[15,29] The variation in the crack length results through the thickness of the specimen (see Figure 42) gives rise to difficulties in specifying the actual crack growth values (the creep test conditions are specified in Table 4).[29]
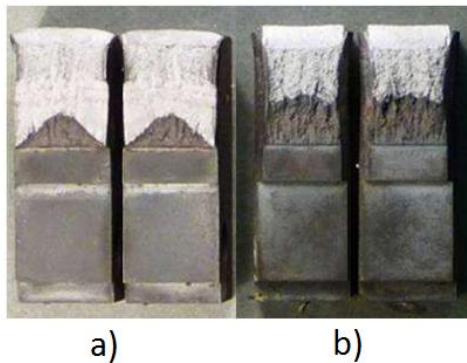
Figure 41. Fracture surface of 316H SS CT specimen indicating a) non-uniform and b) uniform crack growth profile along the thickness due to presence of side grooves.[29]

Tunneling is prevented by the incorporation of side grooves (see Figure 43), also called shear lips, which are manufactured to the ASTM E1457 standard, as shown in Figure 36. Other geometrical feature are also incorporated to the CT specimen geometry (Figure 44).

Table 4. Experimental test conditions and specimen configurations used to describe effect of side grooves.[4]

Specimen	Type	Side groove	Load /N	Duration /h	Δa/mm
CT6	X-weld	10%	1700	1533	5.75
CT9	X-weld	10%	1700	1230	4.10

Figure 42. Variation of crack growth length through the thickness of several 316H steel specimens at 600°C, where 18% denotes $\varepsilon_f = 18\%$.[29]
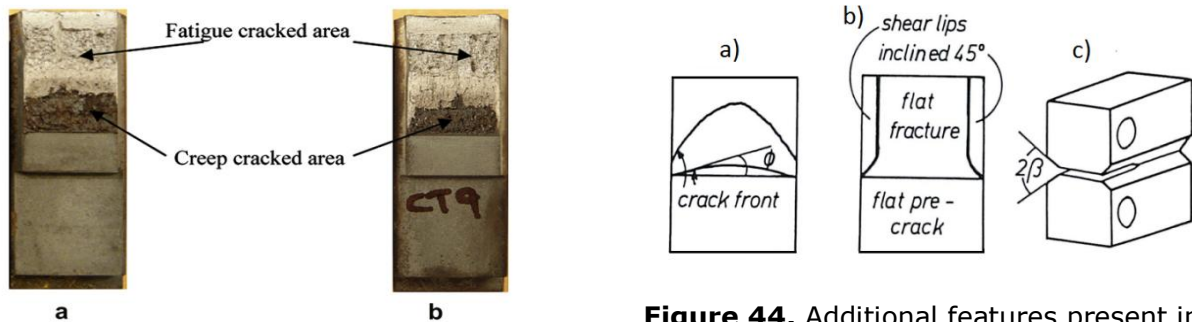
Figure 43. Experimental cracked surface areas of CT6 and CT9 different CT specimens indicating two different types of failure regions.[4]

Figure 44. Additional features present in the CT specimen - b) and c) - in order to reduce the non-uniform crack growth, a).[15]

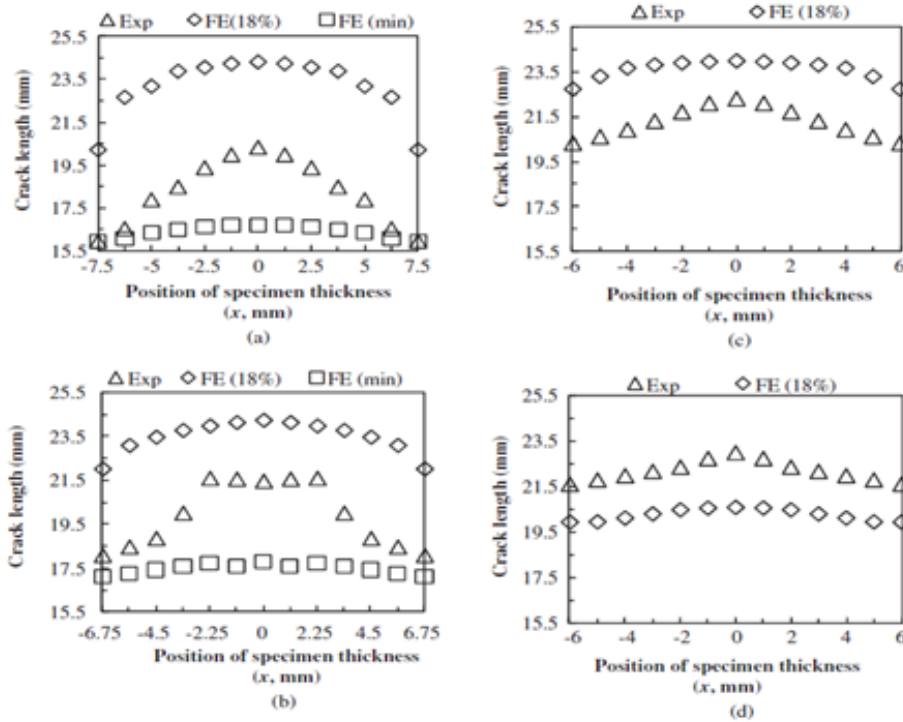Important observation can be made from Figure 43 which indicates two different crack growth regions which resulted after breakage. The darker region is associated with crack growth due to creep deformation, whether the lighter region are the result of fatigue induced deformation, arising from the complete separation of the surfaces at fracture.[4]

The "tail" effect which is used to describe the difference in the initial crack growth rates at the beginning a CT specimen creep testing for different material configurations, as demonstrated in Figure 36, is also of importance when dealing with creep data extracted from CT specimen testing. Consideration should be made of the initial growth rate especially when creep-brittle materials are used.[30]

The geometrical entity and material mismatch of the specimen will affect the steady-state behaviour of the crack under creep conditions when the C*-expression is used - most importantly initial growth and time to failure. Since the empirical expression is

$C*=f(a,W,P,B_N,n,\dot{\Delta}_C)$ specific a/W ratios which account for small differences in the domain configuration of the CT specimen are proposed by the ASTM E1457-13 standard.[30]

Residual stresses that arise within the weld structure can affect the failure life predictions in a CT specimen with tensile ones assisting crack opening and compressive residual stresses reducing the crack growth rate.[37,38] Thus the following residual stress compensation expression for reference stress C*-value is suggested by Nikbin [34]:

$$C^* = \sigma_{ref}\dot{\varepsilon}_{ref}\left(\frac{K_{app} + K_{res}}{\sigma_{ref}}\right)^2 \tag{21}$$

C*-integral procedure and considerations

In order to determine the C*-integral value through FE modelling procedures viscous analysis can be conducted and contours can be specified surrounding the crack tip, which can be either in radial or contour path form (see Figure 45).[32,39,40] Most FE commercial codes, e.g. Abaqus 6.14, include a built-in routine which obtains the transient form C(t)-values of the C*-integral, the latter being the steady-state value (same applies for $\dot{\Delta}_C$).[41] Thus, in order to compute accurate C*-value sufficiently large number of time steps should be specified, since the analysis are time-dependent, as demonstrated in Figure 46. The mesh convergence is also of consideration since the contour integral stress fields exhibit a $1/r^{1/2}$ singularity - see equation (22), as described by Riedel,[15] which leads to the consideration that collapsed elements should be used within the first contour region, surrounding the crack tip.

$$\dot{\sigma}_{ij} = \left(\frac{C^*}{I_n Ar}\right)^{\frac{1}{n+1}} \Sigma_{ij}(\theta,n)\,, r \to 0 \tag{22}$$

$$\dot{\varepsilon}_{ij} = A\left(\frac{C^*}{I_n Ar}\right)^{\frac{n}{n+1}} E_{ij}(\theta,n) \qquad r \to 0 \tag{23}$$
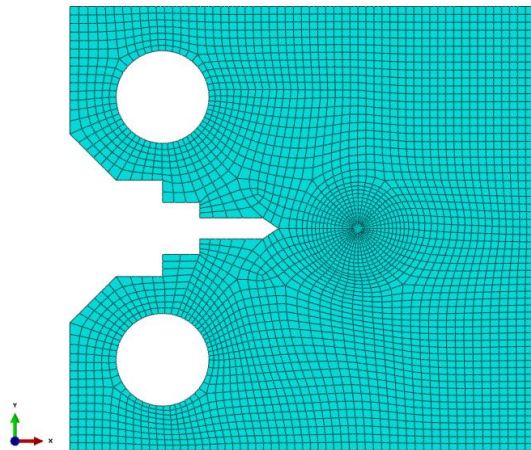

Figure 45. FE mesh used in order to represent circular contours surrounding the crack rather than contour path lengths.
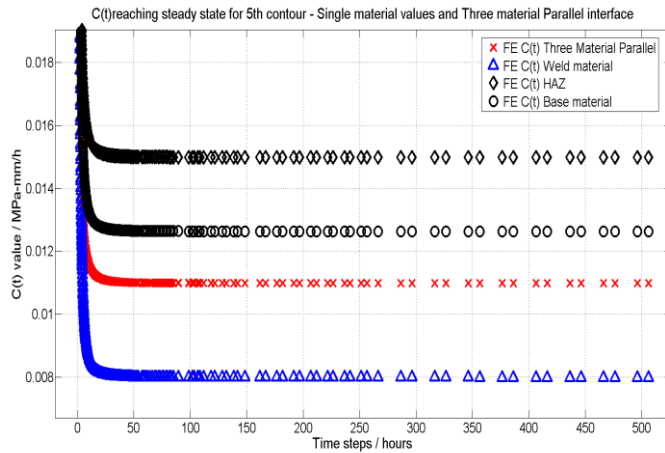
Figure 46. The variation of CT-integral value a circular contour with respect to time for four different material geometry configurations - austenitic 316H weld (close-up view of graph).

The application of the load and its interconnectivity with the model geometry has also an effect on results (see Figure 35). Modelling the system through a Multi-Point constraint between the centre and the nodes at the arc with load applied at the centre, as shown in Figure 47, will lead to reduced computational times. In contrast, load applications directly to the arc or modelling an additional rigid element, e.g. a pin, into an assembly with the CT specimen will result in model which will accurately represent actual test specimen deformations.[4]

The C*-integral is considered to be path-independent and thus can be used to describe CCG response.[3,34] This is observed to be true for all cases in which the CT specimen comprises of a single material such as the parent material (PM) configurations.[4,34,40] However, it should be noted that the C*-integral are also applicable and widely used in other cracked specimen geometries, e.g. DENT plate proposed by Assire et al.[42]

Figure 47. MPC (Multi-Point Constraint) - rigid connection between the centre of the hole and the surrounding nodes of the mesh.

The static form of C*, i.e. J-integral, was derived on the basis that the contour does not cross any material boundaries, i.e. the structure is homogeneous.[35] Considerations should be made of the validity of C*-contour path-independence when applying the integral to a heterogeneous structure, typically welds.[3,33,43,44] The C*-integral is widely utilised in creep analysis of type IV cracks which initiate and grow within a heterogeneous material field.[45] It was shown by Halighongde [40] and Nikbin [34] that for a multi-domain CT specimen consisting of either PM/WM or PM/HAZ/WM with the crack plane being parallel to the material interface the values of C*-integral stay path-independent and do not vary for different contours selected, thus can be used to characterise CCG.[33,34,46] In contrast, if the material interface within the CT specimen is orientated at an angle to the crack plane, the path-independence is observed to

disappear (see Figure 48) with differences of more than 10% across different circular contours,[40] which will results in inaccurate failure time and creep strain predictions.
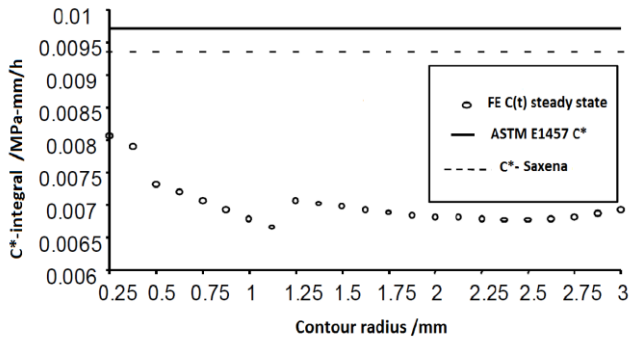

Figure 48. C*-integral values for different contour radii for a three-material weld CT specimen with an angular material interface to the crack plane.[40]

Observations on the path-dependence of creep data for C*-integral for multi-domain structures with angular material interface to the crack plane correlate with similar observations made by Nakagaki et al.[39] and Kikuchi et al.[43] on the static form of C*-integral - J-integral (see Appendix 4).

Comparison between FE computed C*-integral values and ones that are empirically obtained via the ASTM C*-expression has been made via equation (19). The differences between empirical and FE C*-values indicate that the empirical formula is accurate enough as shown in Figure 49 (differences of less than 5%) for single material, e.g. Mn-C steel at 360°C (Figure 50),[36] or two material condition with the material interface parallel to the crack growth direction, i.e. with increasing heterogeneity of the specimen, the applicability of equation (19) becomes invalidated.

Sufficient time interval for the initial static stress deformation to be redistributed to stationary-state creep deformational behaviour has to be considered, as suggested by Nikbin [34] and Davies et al.[47] with a specified CCI extension of 0.2 mm which accounts for the transition time to steady-state CCG, see equation (24).[30]

$$t_{iL} = \frac{\Delta a \varepsilon_f^*}{3 C^{*0.85}}$$
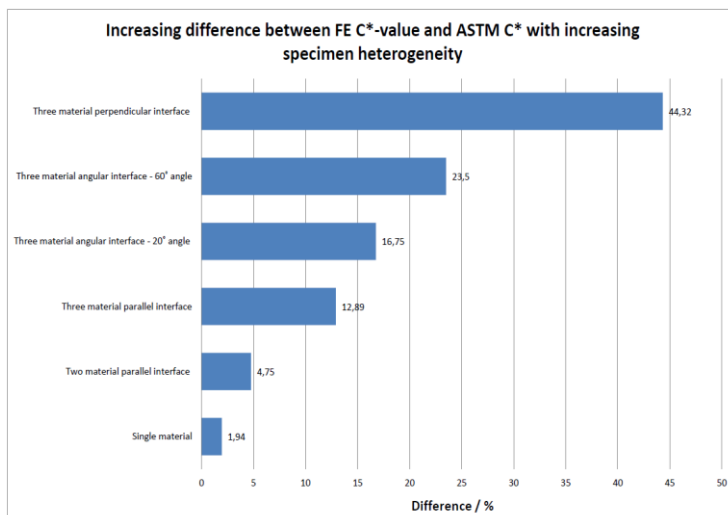(24)

Figure 49. Difference between the FE C* and empirical ASTM C*-value for the 316H six different material configurations.
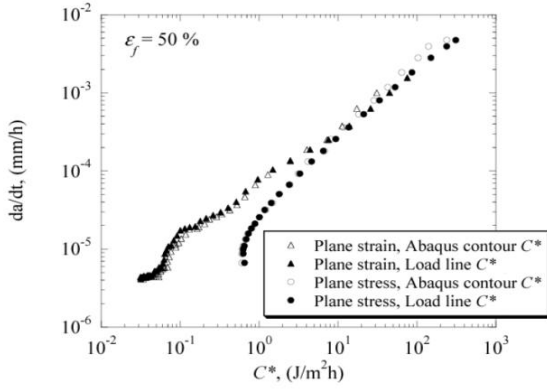
Figure 50. CCG rate for Mn-C steel at 360˚C versus C*-integral values via FE and empirical computation via equation (19).[36]

Modifications of these empirical C*-integral relations are made, taking into account the effect of the material mismatch ratio, M, on the creep exponent, n, and of the variation of η with respect to the weld dimensions, see equation (25). These are suggested as an adjusted model which produces more accurate C*-values for two and three material parallel material interface configurations; the complete procedure is being described in detail by Xuan et al.,[48] as applied to the weld geometry cases shown in Figure 51. The adjusted parameter results in good agreement between the FE and empirically obtained C*-values, but they are more time-consuming.[4] For a soft under-matching weld the adjusted η_W will be greater than the homogeneous value, while for an over-matching weld the resulting η_W will be smaller.[48]

$$C_W^* = \eta_W \frac{n_{eq}}{n_{eq}+1} \frac{P\dot{\Delta}_C}{B_N(W-a)} \tag{25}$$

The use of the C*-integral method for modelling CCG of materials with low fracture strains is not recommended for brittle materials subjected to low stresses in plane strain conditions.[36]
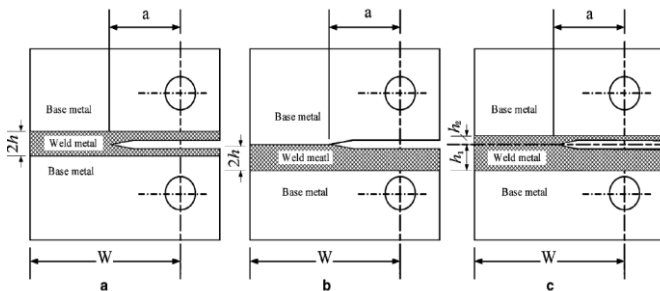
Figure 51. Schematic diagrams of two material mismatched CT specimens - a) weld centre crack, b) interface crack and c) asymmetric crack.[48]

It should be noted that different failure strains can be selected, obtained via different assumptions.[15] A procedure based on the use of mean values of creep failure strain with upper and lower boundaries, estimated to be between 10% and 26%, as suggested by Yatomi et al.[36] Higher creep failure strains can be also used for studies on sensitivity of the results.

Considerations of the damage mechanics approach for CT specimen

The damage mechanics methods, being the Kachanov model and the Liu/Murakami model (equations (1) to (6)), are used to a lesser extent than the C*-contour integral approach due to the complexity of the material models and of the large number of

material constants (see Table 5) that need to be determined.[33] The damage models possess high mesh sensitivity, thus greater computational power and time are required,[40] where a typical 3D FE damage model is shown in Figure 52.

Figure 52. Typical 3D mesh of three material CT specimen used for damage mechanics analyses.[4]

In terms of the component creep life data obtained through the damage-based approaches it tends to give a more accurate representation and provides good correlation with experimental data (see Figures 53 and 54).[4,33]
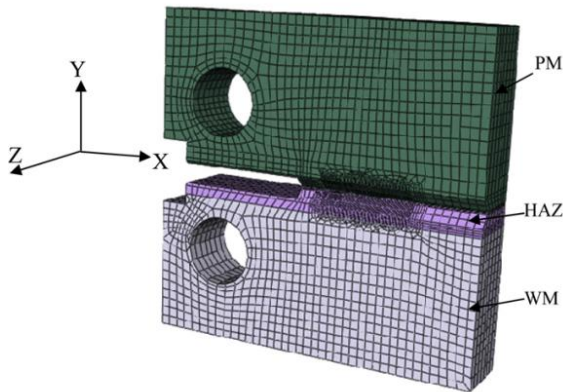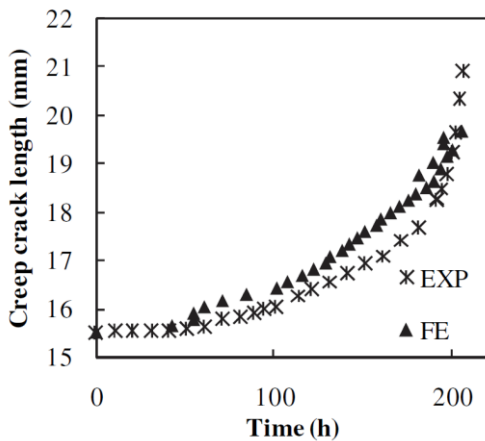

Figure 53. FE creep crack growth rate, obtained via compared to experimental results for a P91 weld at 650°C represented via CT specimen.[4]
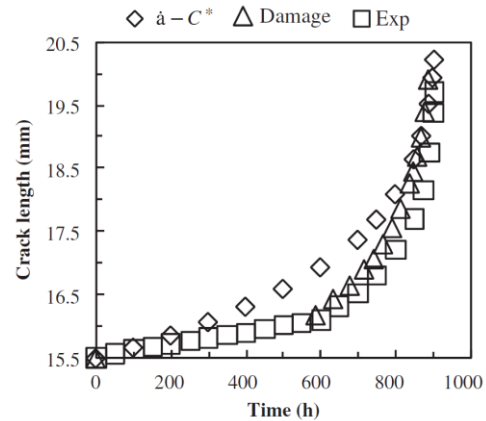
Figure 54. Comparison between crack growth data obtained via experimental, FE C*-method and damage mechanics approach results for a P91 weld at 650°C.[29]

An important consideration should be made based on the fact that a CT specimen represents a cracked geometry and the stress fields, surrounding the crack tip will be intrinsic. A comparison between the Kachanov model and the Liu/Murakami model indicated that the latter is more applicable and accurate to CT specimen CCG characterisation, as stated by Hyde et al.[33] The widely applied and easier to compute Kachanov model results in large localised increases in stress at the crack tip, thus period of the time steps required decreases drastically leading to a nearly singular behaviour of the damage accumulation, i.e. damage rates approaching infinity at $t/t_f \approx 1$, with the creep strains affected to a lesser extent (see Figure 55). On the other hand, the Liu/Murakami method is a more comprehensive procedure that allows for more accurate modelling of the stress states and times to failure (see equation (26)), surrounding the

crack tip, and this should be considered when dealing with damage modelling of CT specimens.[33,49] The time to failure expression given by the Liu/Murakami method[20] is:

$$t_f = \frac{\sigma^{-p}}{D} = \frac{1}{D\big(\alpha\sigma_1 + (1-\alpha)\sigma_{eq}\big)^p} \tag{26}$$

With the current damage state being:

$$\omega = -\frac{ln\left(1 - D(1 - e^{-q_2})t\sigma^p\right)}{q_2} \tag{27}$$

Table 5. Damage mechanics constants for Liu/Murakami model determined for 316 stainless steel at 600°C.[33]

C	n_2	D	p	q_2	α
1.47×10^{-29}	10.147	2.73×10^{-30}	10.949	6.35	0.47845

The above statements are verified through the damage contours obtained, describing the crack fracture, through the thickness of the specimen. Examination of Figure 55 leads to the observation that accurate damage contours at **ω** = 0.99 for CCG predictions via a CT specimen, where large stress concentrations near the crack tip occur, are only possible when the Liu/Murakami parameters have been used (creep conditions are shown in Table 6). Computation of the damage contours in Figure 56 would have been impossible to obtain through the application of the Kachanov model, as described by Hyde et al.[4,33] This observation is also verified via thumbnail CCG specimen modelling, as shown in Figure 57. Consideration should also be made when a fine mesh is used for damage modelling with plastic behaviour in front of the crack tip, incorporated to the model, since the effect of plasticity may reduce the creep strain rates and crack tip region triaxiality, as observed by Yatomi et al.[36]

Observations of crack growth predictions obtained via the damage models, conducted through node-release result in higher values than estimations using fixed-node models, especially in plain strain conditions, as described by Yatomi et al.[36] and Hyde et al.[33], indicating that using different types of node system will affect the creep behaviour of the crack.

With regards to the material constants it should be noted that the chosen triaxiality parameter, **α**, affects damage predictions and their correlation with the experimental data, since the multi-axial **α** is determined from experimental tests,[33] but conventional biaxial experimental test for determination can be complicated.[50] It is also observed that the triaxiality parameter, α_H, for the weak HAZ of the system is difficult to obtain and is time consuming.[4]
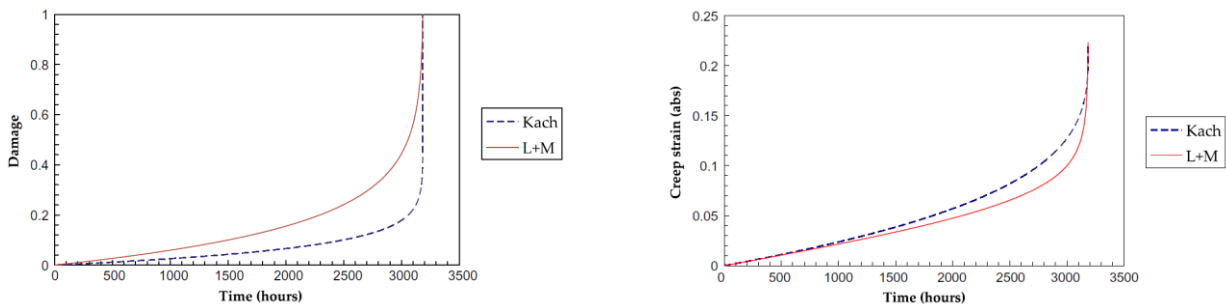

Figure 55. Comparison between uniaxial damage data and creep strain obtained via Liu/Murakami and Kachanov damage models for 316 SS at 600°C.[33]

Table 6. Experimental testing conditions at 600˚C of the three 316 stainless steel CT specimens used to compare damage mechanics predictions to experimental data.[33]

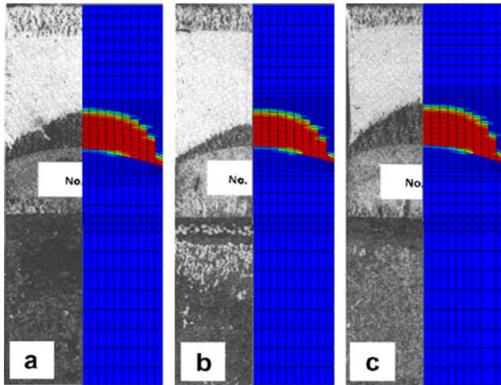| Spec. No.	Load / kN	Duration /h
a) CT spec.	8.522	168
b) CT spec.	6.977	892
c) CT spec.	7.476	504

Figure 56. Tested specimen photo to FE damage contour comparisons for a three CT specimens (see Table 6), showing the **ω** = 0.99 crack zones for **α**=0.48.[33]
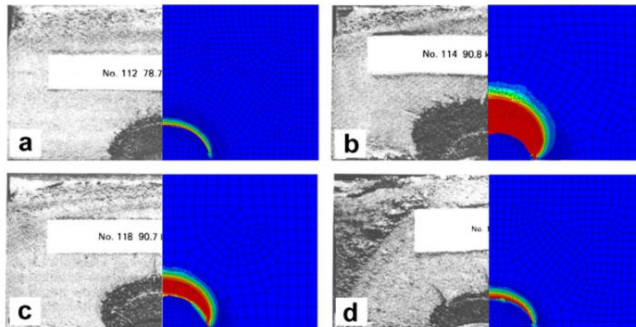
Figure 57. Tested specimen photo to FE damage contour comparisons for four thumbnail crack specimens at **ω** = 0.99.[33]

Comparison has been made in order to investigate how the damage model corresponds to experimental and fracture mechanics (e.g. C*-integral) crack growth predictions by Hyde et al.[29] From Figure 54 it is observed that the damage mechanics Liu/Murakami correlates better to the experimental data for a P91 weld at 650˚C than the $\dot{a} - C^*$ approach. Although the Liu/Murakami damage model is more accurate, due to its complexity it is not widely used in industry.

Higher accuracies of CCG predictions using both $\dot{a}$-C* approach and Liu/Murakami models can be obtained by using greater number of time intervals specified and further mesh refinement, however this will increase the time of the creep analysis.[40]

Considerations of CT specimen stress field orientation and applicability

Considerations have to be made of the stress field and loading orientation of a conventionally tested CT specimens with regards to their use for CCG behaviour of internally pressurised thick pipes. The compact tension specimens are loaded with a point force at the both holes and it should be noted that this is an idealised loading condition.

A small element extracted from a thick pipe will experience uniformly-distributed pressures at its interfaces (see Figure 58), rather than point force constraints, although uniform stress loading at the interface will not invalidate the theory - e.g. C*-integral values will stay path-independent for uniform pressure loading at the interfaces, but C^*_{Force} and $C^*_{Pressure}$ will differ (see Figures 59 and 60) - thus standardised procedures should always be followed and creep life estimation CT specimen data should be applied with care to real life conditions.[30,31,51]
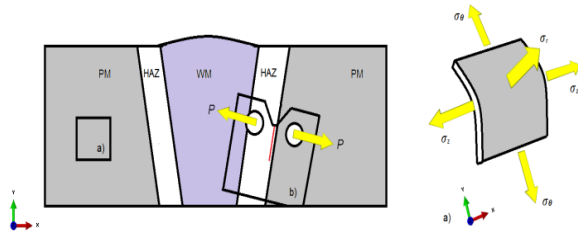

Figure 58. Schematic diagram of an extracted CT specimen (b) from a pipe weld with Type IV crack and the point force, P, applied at both holes. The three stresses arising in a small element of the pipe (a) are also shown.

Another important observation made on the stress fields of a crack in an internally pressurised thick pipe, which can also relate back to cross-weld specimens, is that stress in three directions are present - σ_θ, σ_z and σ_r - while conventional testing will comprise of loading only in one direction.[1] Consideration should be taken into account that biaxial experimental testing can also be carried out, with the procedures are complicated and expensive, but CCG predictions will be closer to real-life behaviour.
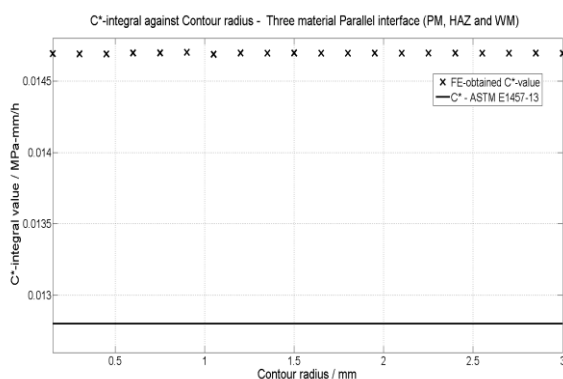
Figure 59. FE and empirical ASTM C*-integral values, equation (19), for different contour radii - single material (PM) CT specimen - 5 kN Point force loading.
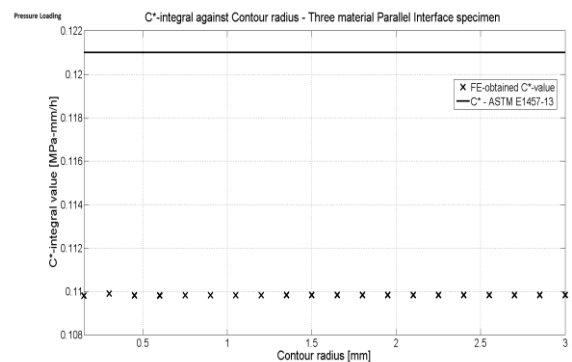
Figure 60. FE and empirical ASTM C*-integral values, equation (19), for different contour radii for a three material parallel interface (PM, HAZ and WM) CT specimen - 100 MPa Pressure loading at interfaces.

Summary of complications to the use of CT specimen modelling

In this section it has been shown that even for the simple geometry and loading conditions which exist for CT specimens the stress and deformation conditions are highly complicated. The factors which influence the behaviour of such specimens include:

- Material behaviour (models used range from Norton power law to more realistic models like the Liu/Murakami models)
- CT specimen $\dot{a}$-C* data is not necessarily in the same loading state as that of the component to which it is applied

- Path-dependence of C* arising due to material heterogeneity
- A damage approach allows crack initiation as well as CCG to be investigated
- The C*-contour integral approach is based on a singularity that exists in front of the crack tip. CCG predictions are highly-dependent on the mesh, surrounding the crack tip.
- CT specimen $\dot{a}$-C* data varies for plane strain and plane stress conditions
- Damage mechanics models require a greater number of material constants to be computed than the C*-contour integral fracture mechanics approach.

Discussion and Future work

This paper shows that cross-weld and compact tension specimens can accurately describe the bulk creep behaviour, creep crack growth behaviour and failure modes of welded joints. Creep analysis and data extracted from cross-weld specimens have shown that the most common Type IV cracking failure mode can be precisely modelled via the Liu/Murakami and Kachanov damage mechanics models, and creep modelling of CT specimens accurately represent creep crack growth behaviour of heterogeneous structures via using both the C*-contour integral fracture mechanics parameter and Liu/Murakami damage mechanics model.

However, in cross-weld specimen modelling, significant differences between the predicted creep life and the real life of a component may arise due to incorrectly modelled stress field within the cross-weld specimen relative to welding direction as well as the anisotropy of the weld material. Stress singularities present in the heterogeneous material interface and the different weld angles relative to the loading direction also give rise to discrepancies in the predicted creep failure lives and positions. On the other hand, creep crack growth predictions obtained from CT specimen testing via both fracture mechanics C*-contour integral and damage mechanics Kachanov model and Liu/Murakami model show good agreement with experimental data and real life component behaviour. The Liu/Murakami damage model has been identified as being more applicable to creep crack growth characterisation and damage rate analysis than the Kachanov model - the latter is simpler than the Liu/Murakami method in terms of computation, but gives rise to large stress concentrations at the crack tip being impossible to model. On the other hand, the C*-contour integral method provides a feasible way of characterising creep crack growth behaviour, easier than the Liu/Murakami model in terms of computation as only *A* and *n* material creep constants are required. However, the C*-contour integral path-independence is observed to be strongly dependent on the material interface orientation with respect to the crack plane and the loading state of the specimen, thus it becomes invalidated in certain conditions.

This article suggests that the correct alignment of the stress fields directions of the weld (longitudinal and transverse) and the corresponding hoop and axial directions within a steam pipe to cross-weld specimens with regards to the actual geometry and material mismatch of the component should be examined in more depth. Also the residual stresses induced in multi-pass welds and their effect on the failure behaviour of the specimen should be further investigated. The standard loading states of compact tension specimens with respect to actual stress state of actual components should also be considered in more detail as should the applicability and validity of the commonly used C*-contour integral with respect to the heterogeneous material interface orientation. The creep behaviour data and observations, obtained by CT specimen modelling via both damage and fracture mechanics models, described in this study suggest that biaxial stress state modelling and the use of other models, describing material behaviour, should also be studied to allow more extensive use of such specimen models for the characterisation of other heterogeneous material structures.

References

[1]. Hyde T.H., Hyde C.J. and Sun W., Applied Creep Mechanics, McGraw-Hill Education, 2014.

[2]. Hyde T.H., Sun W., Agyakwa P.A., Shipway P.H., and Williams J.A., Anisotropic creep and fracture behaviour of a 9CrMoNbV weld metal at 650°C, *Anisotropic behaviour of damaged materials*, 2002, Chapter 9, pp.295-316, eds. J.J.Skrzypek and A.Ganczarski, Springer Verlag, Berlin Heidelberg.

[3]. Davies C.M., Dean D.W., Nikbin K.M., and O'Dowd N.P., Interpretation of creep crack initiation and growth data for weldments, *Engineering Fracture mechanics*, 2007, **74**(6), pp.882-897.

[4]. Hyde T.H., Saber M. and Sun W., Creep crack growth data and prediction for a P91 weld at 650°C, *Int. Journal of Pres. Vessels and Piping*, 2010, **87**(12), pp.721-729.

[5]. Hyde T.H. and Sun W., A method for estimating the stress distribution on the centre line of an axisymmetric two-material creep test specimen, *Int. J. Mech. Sci.*, 1997, **39**(8), pp.885-898.

[6]. Schuller H.J., Hagn L., and Woitscheck A., Cracking in the weld region of shaped components in hot steam pipelines - materials investigations, *Der Maschinenschaden*, 1974, **47**(1), pp.1-13.

[7]. Hyde T.H., Sun W., and Williams J.A., Creep analyses of pressurized circumferential pipe weldments - a review, *J. Strain Analysis*, 2003, **38**(1), pp.1-27.

[8]. Hyde T.H. and Sun W., Creep of Welded Pipes, *Proceedings of the IMechE*, 212, Part E, *J.Mech.Processing Eng.*, 1998, pp.171-182.

[9]. Hyde T.H. and Sun W., Some issues on creep damage modelling of welds with heterogeneous structures, *Int. J. Mech.Mater.Des.*, 2009, **5**(4), pp.327-335.

[10]. Hyde T.H., Becker A.A., Sun W., Yaghi A., Williams J.A., and Concari S., Determination of creep properties for P91 weldment materials at 625°C, *5th International Conference on Mechanics and Materials in Design*, 2006, Chapter IV: Welds at High Temperature in Design, Porto, Portugal.

[11]. Hyde T.H. and Sun W., Creep failure behaviour of a 9CrMoNbV weld metal with anisotropy under a biaxial loading state, *J.Strain Analysis*, 2006, **41**(5), pp.369-380.

[12]. Hyde T.H., Sun W., and Becker A.A., Effect of geometry change on the creep failure life of a thick-walled CrMoV pipe with a circumferential weldment, *Int. J. Press. Vessels and Piping*, 2004, **81**(4), pp.363-371.

[13]. Dogan B. and Petrovski B., Creep crack growth of high temperature weldments, *Int. Journal of Pressure Vessels and Piping*, 2001, **78**(11-12), pp.795-805.

[14]. Hyde T.H. and Sun W., A study of anisotropic creep behvaiour of a 9CrMoNbV weld metal using damage analyses with a unit cell model, *J. of Materials: Design and Applications*, 2005, **219**(4), pp.193-206.

[15]. Riedel H., Fracture at high temperature, Springer-Verlag Berlin, Heidelberg, 1987.

[16]. Tanner D.W.J., Sun W., and Hyde T.H., The effect of weld fusion zone angle in a cross-weld specimen under creep, *12th Int. Conference on Creep and Fracture of Eng. Mats. and Strus.*, 2011, Japan, May 22-27.

[17]. Hyde T.H. and Sun W., Effect of bending load on the creep failure behaviour of a pressurised thick walled CrMoV pipe weldment, *Int.J.Pressure Ves. and Piping*, 2002, **79**(5), pp.331-339.

[18]. Hyde T.H., Sun W., Becker A.A., and Williams J.A., Creep continuum damage constitutive equations for the base, weld and heat-affected-zone materials of a service-aged 1/2Cr1/2Mo1/4V:2 1/4Cr1Mo multi-pass weld at 640°C., *J. Strain Analysis*, 2005, **32**(4), pp.193-206.

[19]. Kachanov L.M., Theory of Creep (English Translation edited by A.J.Kennedy), National Lending Library, Boston Spa, 1960.

[20]. Liu Y. and Murakami S., Damage localization of conventional creep damage models and proposition of a new model for creep damage analysis, *JMSE International Journal*, 1998, **41**(1), pp.57-65.

[21]. Hyde T.H. and Sun W., Stress singularities at the free surface of an axisymmetric two-material creep test specimen, *J. Strain Analysis*, 1997, **32**(2), pp.107-117.

[22]. Hyde T.H., Sun W., Becker A.A., and Williams J.A., Effect of weld angle and axial load on the creep failure behaviour of an internally pressurised thick walled CrMoV pipe weld, *Int.J.Pressure Ves. and Piping*, 2001, **78**(5), pp.365-372.

[23]. Hyde T.H., Williams J.H. and Sun W., Assessment of creep behaviour of narrow gap welds, *Int. J. Pressure Vessels and Piping*, 1999, **76**(8), pp.515-525.

[24]. Hall F.R. and Hayhurst D.R., Continuum damage mechanics modelling of a high temperature deformation and failure in a pipe weldment, *Proc. R. Soc. London*, 1991 A443, pp.383-403.

[25]. Hyde T.H., Becker A.A., Sun W., Yaghi A., Thomas A., and Seliger P., Finite element creep failure analyses of P91 large tensile cross-weld specimens tested at 625°C, *5th Int. Conf. on Mechanics and Materials in Design*, 2006, University of Porto, Portugal, July 24-26.

[26]. Elmesalamy A., Francis J.A. and Li L., A comparison of residual stresses in multi pass narrow gap laser welds and gas-tungsten arc welds in AISI 316L stainless steel, *Int. Journal of Press. Vessels and Piping*, 2014, **113**(1), pp.49-59.

[27]. Okada T., Ikushima K., Itoh S., Shibahara M. and Nishikawa S., Residual Stress Analysis of Multi-pass welding using idealized explicit FEM with GPU, *Transactions of JWRI*, 2011, Special Issue on WSE2011, pp.93-94.

[28]. Thomas, A., Pathiraj, B., and Veron, P., Feature tests on welded components at higher temperatures - Material performance and residual stress evaluation, *Engineering Fracture Mechanics*, 2007, **74**(6), pp.969-979.

[29]. Hyde T.H., Li R., Sun W., and Saber M., A simplified method for predicting the creep crack growth in P91 welds at 650°C, *Proc.IMeche*, 2010, **224**(1), pp.208-219.

[30]. ASTM standards, E1457-13, Standard test methods for measurements of CCG rates in metals, 2000.

[31]. R6: Assessment of the integrity of structures containing defects. *British Energy*, R/H/R6-Revision - 4, 2001.

[32]. ABAQUS, T.B., Fracture mechanics study of a compact tension specimen using ABAQUS/CAE, 2004.

[33]. Hyde C.J., Hyde T.H., Sun W., and Becker A.A., Damage mechanics based predictions of creep crack growth in 316 stainless steel, *Engineering Fracture Mechanics*, 2010, **77**(12), pp.2385-2402.

[34]. Nikbin K.M., Evaluating creep cracking in welded fracture mechanics specimens, *Engineering Fracture mechanics*, 2007, **74**(6), pp.853-867.

[35]. Rice J. and Rosengren. G.F., Plane strain deformation near a crack tip in a power-law hardening material, *J.Mech.Phys.Solids*, 1968, **16**(1), pp.1-12.

[36]. Yatomi M., Nikbin K.M. and O'Dowd N.P., Creep crack growth prediction using a damage based approach, *Int. J. Pressure Vessels and Piping*, 2003, **80**(7-8), pp.573-583.

[37]. Lei Y., O'Dowd N.P., and Webster G.A., Fracture mechanics analysis of a crack in a residual stress field, *Int. J. Fract.*, 2000, **106**(3), pp.195-216.

[38]. Muránsky O., Bendeich P.J., Smith M.C., Hossienzadeh F., and Edwards L., Numerical analysis of retained residual stresses in C(T) specimen extracted from a multi-pass austenitic weld and their effect on crack growth, *Engineering Fracture Mechanics*, 2014, **126**(1), pp.40-53.

[39]. Nakagaki M. and Miyazaki N., Two-dimensional finite element analysis of stably growing cracks in inhomogeneous materials*, International Journal of Press. Vess. and Piping*, 1995, **63**(3), pp.249-260.

[40]. Halighongde S., Simulation of High Temperature Crack Growth in Welds using Finite Element analysis, PhD Thesis, University of Nottingham, 2009.

[41] Saxena A., Creep crack growth under non-steady state conditions, *Fracture Mechanics: ASTM STP 905*, American Society for testing and materials (ASTM), 1986, **17**(1), pp.185-201.

[42]. Assire A., Michel B., and Raous M., Creep crack initiation and creep crack growth assessments in welded structures, *Nucl.Eng.Design*, 2001, **206**(1), pp.45-56.

[43]. Kikuchi M., Miyamoto H., and Sugawara S., Evaluation of J-integral of a crack in a pressure vessel under thermal transient loadings, *Journal of Press. Vessel Technology*, 1986, **108**(3), pp.312-319.

[44]. Budden P.J., and Curbishley I., Assessment of creep crack growth in dissimilar metal welds, *Nucl.Eng.and Design*, 2000, **197**(1-2), pp.13-23.

[45]. Davies C.M., Kourmpetis M., O'Dowd N.P., and Nikbin K.M., Experimental evaluation of J and C* parameter for a range of cracked geometries, *Journal of ASTM International*, 2006, **3**(4).

[46]. Shibli I.A. and Le Mat Hamata N., Creep crack growth in P22 and P91 welds - overview from SOTA and HIDA projects, *Int. J. Press. Vessels and Piping*, 2001, **78**(11-12), pp.785-793.

[47]. Davies C.M., O'Dowd N.P., Dean D.W., Nikbin K.M., and Ainsworth R.A., Failure assessment diagram analysis of creep crack initiation in 316H stainless steel, *Int. J. Press. Vessels and Piping*, 2003, **80**(7-8), pp. 541-551.

[48]. Xuan F.Z, Tu S.T., Wang Z., A modification of ASTM E1457 C* estimation equation for compact tension specimen with a mismatched cross-weld, *Engineering Fracture Mechanics*, 2005, **72**(17), pp.2602-2614.

[49]. Hayhurst R.J., Vakili-Tahami F., Mustata R., and Hayhurst D.R., Thickness and multi-axial stress creep rupture criteria of the Type IV component of a ferritic steel weld, *Journal of Strain Anal. Engng. Des.*, 2004, **39**(6), pp.729–743.

[50]. Hayhurst D.R., Creep rupture under multi-axial states of stress, *J.Mech. Phys. Solids*, 1972, **20**(6), pp.381-382.

[51]. Nikbin K.M., Creep/Fatigue crack growth testing, modelling and component life assessment of welds, *Procedia Engineering*, 2013, **55**, pp.380-393.

[52]. Hull D. and Rimmer D.E., The growth of grain-boundary voids under stress, *Phil.Mag.*, 1959, **4**(42), pp.673-687.

[53]. Westergaard H.M., Bearing Pressures and Cracks, *Journal of Applied Mechanics*, 1939, **6**(1), pp.49-53.

[54]. Irwin G.R., Fracture dynamics, *Fracture of Metals*, 1948, **3**(2), pp.147-166, American Society of Metals, Cleveland, OH.

[55]. Ainsworth, R.A., The assessment of defects in structures of strain hardening material, *Engineering Fracture Mechanics*, 1984, **19**(4), pp.633-642.

Appendix 1

Creep fracture occurs from the nucleation, growth and interlinking of existing flaws and the formation of cavities within the microstructure, as described by Riedel.[15] The empirical relation which describes cavity growth was determined by Hull and Rimmer in equation (28),[52] where J_v is the flux of the cavity and Ω is the atomic volume:

$$J_v = -\frac{D_{gb}}{\Omega kT}\nabla f \tag{28}$$

Thus the cavity growth and CCG is controlled by surface diffusion, plasticity or coupled diffusion and plasticity.

Appendix 2

The damage rate expression, equation (5), in the Liu/Murakami model can be rearranged as follows:

$$\dot{\omega} = \frac{d\omega}{dt} = \frac{D(1-e^{-q_2})\sigma^p e^{\omega q_2}}{q_2} \tag{29}$$

Equation (29) then becomes:

$$\frac{d\omega}{e^{\omega q_2}} = \frac{D(1-e^{-q_2})\sigma^p}{q_2}dt \tag{30}$$

Since the right hand side of the expression is comprised of constant terms (D, q_2, p and σ):

$$\frac{d\omega}{e^{\omega q_2}} = Qdt \tag{31}$$

where

$$Q = \frac{D(1 - e^{-q_2})\sigma^p}{q_2}$$

(32)

By integrating both sides with respect to ω and t respectively the damage, ω, is obtained as follows:

$$\int_0^\omega \frac{d\omega}{e^{\omega q_2}} = \int_0^t Q dt$$

(33)

giving

$$\omega = -\frac{\ln(1 - Qtq_2)}{q_2}$$

(34)

Equation (34) is thus the expression for ω which is required for the creep strain, ε^c, to be a function of time, agreeing with Hyde et al.[1]

Appendix 3

The size of the plastic zone in front of the crack tip may be obtained by substitution of the von Mises stress criterion into the expressions, proposed by Westergaard [53]:

$$\sigma_{xx} = \frac{K_I \cos\left(\frac{1}{2}\right)\theta_1 \left(1 - \sin\left(\frac{1}{2}\right)\theta_1 \sin\left(\frac{3}{2}\right)\theta_1\right)}{\sqrt{2\pi r_1}}$$

(35)

$$\sigma_{yy} = \frac{K_I \cos\left(\frac{1}{2}\right)\theta_1 \left(1 + \sin\left(\frac{1}{2}\right)\theta_1 \sin\left(\frac{3}{2}\right)\theta_1\right)}{\sqrt{2\pi r_1}}$$

(36)

$$\sigma_{xy} = \frac{K_I}{\sqrt{2\pi r_1}}\sin\left(\frac{1}{2}\right)\theta_1.\cos\left(\frac{1}{2}\right)\theta_1.\cos\left(\frac{3}{2}\right)\theta_1$$

(37)

For Mode I opening, the radius of the plastic zone, as proposed by Irwin,[54] in front of the tip is given by:

$$r_p = \frac{K_I^2}{2\pi\sigma_y^2}$$

(38)

Appendix 4

Rice and Rosengren derived the J-integral which describes the energy release rate of the material with the variation in crack length.[35] The J-integral is a contour integral, which is used to describe the behaviour of elastic-plastic materials. The integral was derived from the potential energy variation with crack length as shown below and it is termed and used as being path-independent.[55] Figure 61 shows a schematic representation of the contour and its relation to the crack.

$$\Pi = \left(\int_A W da - \int_S \boldsymbol{T}.\boldsymbol{u} dS\right)t = \left(\int_A W dA - \int_S T_i u_i dS\right)t$$
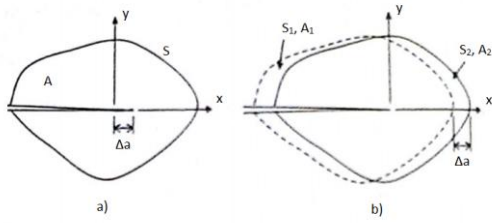
(39)

Figure 61. Schematic representation of the shifting of the control volume, a), with a crack increment, Δa, b).[15]

And the expression for J-integral was determined to be:

$$J = \int_S \left(W dy - T_i \frac{du_i}{dx_i} dS \right)$$

(40)